Journal of Rock Mechanics and Geotechnical Engineering xxx (xxxx) xxx

Contents lists available at ScienceDirect

Journal of Rock Mechanics and Geotechnical Engineering

journal homepage: www.jrmge.cn

Full Length Article

# Multistate transition and coupled solid–liquid modeling of motion process of long-runout landslide

Yang Gao [a,b,*], Yueping Yin [c], Bin Li [a,b], Han Zhang [d], Weile Wu [d], Haoyuan Gao [a,b]

[a] Institute of Geomechanics, Chinese Academy of Geological Sciences, China Geological Survey, Beijing, 100081, China
[b] Key Laboratory of Active Tectonics and Geological Safety, Ministry of Natural Resources, Beijing, 100081, China
[c] China Institute of Geological Environment Monitoring, China Geological Survey, Beijing, 100081, China
[d] School of Geological Engineering and Geomatics, Chang'an University, Xi'an, 710054, China

ARTICLE INFO

*Article history:*
Received 30 May 2023
Received in revised form
29 October 2023
Accepted 4 December 2023
Available online xxx

*Keywords:*
Long-runout landslide
Multistate transition
Mixed solid–liquid flow
Post-failure process
Numerical simulation

ABSTRACT

The recognition, repetition and prediction of the post-failure motion process of long-runout landslides are key scientific problems in the prevention and mitigation of geological disasters. In this study, a new numerical method involving LPF$^{3D}$ based on a multialgorithm and multiconstitutive model was proposed to simulate long-runout landslides with high precision and efficiency. The following results were obtained: (a) The motion process of landslides showed a steric effect with mobility, including gradual disintegration and spreading. The sliding mass can be divided into three states (dense, dilute and ultradilute) in the motion process, which can be solved by three dynamic regimes (friction, collision, and inertial); (b) Coupling simulation between the solid grain and liquid phases was achieved, focusing on drag force influences; (c) Different algorithms and constitutive models were employed in phase-state simulations. The volume fraction is an important indicator to distinguish different state types and solid–liquid ratios. The flume experimental results were favorably validated against long-runout landslide case data; and (d) In this method, matched dynamic numerical modeling was developed to better capture the realistic motion process of long-runout landslides, and the advantages of continuum media and discrete media were combined to improve the computational accuracy and efficiency. This new method can reflect the realistic physical and mechanical processes in long-runout landslide motion and provide a suitable method for risk assessment and pre-failure prediction.



## 1. Introduction

Long-runout landslides are among the most spectacular and catastrophic natural events, and they affect landscapes, populations, and infrastructure in mountainous areas worldwide (Voight and Pariseau, 1978; Cruden and Varnes, 1996; Evans and DeGraff, 2002). The recognition, repetition and prediction of the post-failure motion process of long-runout landslides are key scientific research areas in the prevention and mitigation of geological disasters. These types of landslides exhibit the characteristics of having an immense volume, high-speed, and long-runout distance. In the post-failure motion process, the phase state of the sliding main body is random and variable, including multistate transitions and solid–liquid coupling. This phenomenon can hardly be captured in the field and is difficult to restore in physical modeling experiments due to size limitations. However, long-runout landslides should be quantitatively analyzed.

In recent years, geological, dynamic and numerical models have been rapidly developed, and their purpose is to accurately assess motion processes. Currently, most numerical simulation techniques tend to use a single phase-state algorithm. Based on the macroscopic physical-mechanical state of the sliding main body, the main methods can be classified into the following three kinds: (a) The movement of a sliding main body is simplified to a solid block. This modeling has been employed to analyze deformation between the sliding main body and the underlying surface (Heim, 1932; Scheidegger, 1973). The finite element method (FEM) was used at the slope instability stage, but this method cannot be adopted to effectively simulate large deformation and velocity gradient changes. The discrete element method (DEM) (the Hertz–Mindlin

* Corresponding author. Institute of Geomechanics, Chinese Academy of Geological Sciences, China Geological Survey, Beijing, 100081, China.
*E-mail address:* gaoyangCGS@hotmail.com (Y. Gao).

Peer review under responsibility of Institute of Rock and Soil Mechanics, Chinese Academy of Sciences.

https://doi.org/10.1016/j.jrmge.2023.12.001

model with bonding or linear cohesion modeling) and discontinuous deformation analysis (DDA) can be used to simulate a solid sliding block and the disintegration process (Hrennikoff, 1941; Courant, 1943; Shi, 1992; Banton et al., 2009; Wu and Wong, 2014; Zhang et al., 2012) but are computationally inefficient; (b) Following the pioneering work of Bagnold (1954), granular flow modeling without the need for interstitial fluid has become an important research area, and this type of modeling distinguishes between frictional and collision regimes (Melosh, 1986; Campbell, 1989). Granular flow simulation mainly uses the discrete media of the DEM. The Newtonian law of mechanics and the interparticle contact model have been applied to calculate friction and collision processes (partial flow code (PFC) and matrix computing of the DEM (MatDEM)) (Cundall and Strack, 1979; Liu et al., 2017). This modeling can meet the calculation accuracy requirements, but the calculation efficiency is low, and the actual number of landslide particles can hardly be simulated; and (c) The concept of equivalent fluid modeling, which was introduced by Hungr (1995), expresses the movement characteristics of rapid and long-runout flow-like landslides, and the basal friction resistance and flow mass lateral pressure greatly contribute to the motion process (Erismann and Abele, 2001; Crosta et al., 2009; Sassa et al., 2010). These methods are mainly based on Eulerian and Lagrangian computational fluid dynamics. This type of modeling mainly involves meshless particle and grid methods (smoothed particle hydrodynamics (SPH), lattice Boltzmann method (LBM), and material point method (MPM)) (Gingold and Monaghan, 1977). This modeling approach provides high computational efficiency, but the computational accuracy is relatively low and greatly depends on the parameter experience of geologists. The natural motion process of the sliding main body is random and variable and reflects the multiphase state. The single-phase state exhibits certain limitations in fully capturing the realistic physical mechanic process of long-runout landslides.

In the post-failure motion process, fragmentation and spreading of the sliding main body cause a change from a rockslide to a debris avalanche. Under high-rainfall conditions, debris grains are mixed with ground surface runoff and are converted into a solid–liquid mixed flow, such as a debris flow or debris flood. Numerical algorithms for the single-phase state must be studied in more detail toward the multiphase state. Presently, multiphase-state simulation methods mainly include the following: (a) In continuum theories of granular flow, the fluctuation energy is regarded as an independent state variable (Haff, 1983; Hutter and Rajagopal, 1994; Louge and Keast, 2001; Louge, 2003). Algorithmic conversion techniques have also gradually been developed to accurately simulate the dynamic processes of long-runout landslides, such as the static solid to dynamic granular flow transition in the FEM-DEM algorithm (Feng et al., 2014); and (b) Multiphase flow is generally simulated using DEM-computational fluid dynamics (DEM-CFD) and DEM-SPH coupling algorithms (Shan and Zhao, 2014; Tan and Chen, 2017; Tan et al., 2018; Jing et al., 2019; Yang et al., 2020; Morikawa and Asai, 2022). In regard to mixed two-phase flow landslides, not only fluid and solid dynamics but also the interactions between these two phases must be considered (Kelfoun et al., 2010). The DEM-CFD coupling model has been used to study the mechanical and fluid behavior of liquid–solid fluidized bed systems, air–grain mechanical systems, and liquid–grain submarine landslides (Zbib et al., 2018; Drame et al., 2021). In existing simulation methods that span multiple states, numerical calculations are used for coupling purposes. However, these methods cannot accommodate the selection of various macroscopic mechanical constitutive and simulation parameters in different phase states. The DEM must be calibrated to match the macroscopic mechanical constitutive model, while the macroscopic continuous medium algorithm based on hydrodynamic equations is insufficient for calculating collision and friction. Numerical modeling must be adjusted to suit the actual landslide movement process. This can be achieved by incorporating different algorithms and constitutive models in phase-state simulations.

In this study, a multistate transition and solid–liquid coupling dynamics modeling technique was developed, including a new numerical simulation method for long-runout landslides. The proposed method could overcome the high computational complexity and the inability to obtain macroscopic characteristics of traditional versions of the DEM, and full three-dimensional simulations could be realized to improve efficiency and accuracy. Based on the transition and coupling between different algorithms (SPH, smoothed discrete particle hydrodynamics (SDPH), and DEM) and different constitutive models (fluid mechanics model, elastic–viscoplastic model, Hertz–Mindlin contact model, and kinetic model of granular flow), the landslide post-failure process in a three-dimensional computing platform ($LPF^{3D}$) was proposed. Flume experiments with dry granular flow and mixed solid–liquid flow conditions were used to verify the dynamic numerical modeling results and validate the algorithm parameters. The long-runout landslide cases in the southwest mountainous area of China were selected to demonstrate that the developed numerical simulation method can efficiently and accurately simulate the post-failure motion process. This new method could reflect the physical and mechanical processes in long-runout landslide motion and provide a suitable method for risk assessment and pre-failure prediction.

## 2. Geological mechanics model

The material type of the sliding main body plays a crucial role in landslide classification and post-failure motion processes (Varnes, 1958, 1978; UNESCO, 1981, 1993; Hungr et al., 2014). In the numerical simulation of long-runout landslides, it is necessary to choose different algorithms and constitutive models according to the different material types and motion states. Therefore, long-runout landslides can be divided into three main types from a numerical simulation perspective according to the deposition characteristics, material types, and material components (Coussot and Meunier, 1996; Takahashi, 2007; Gusman et al., 2009; Zhou et al., 2020; Yin et al., 2023). The aim was to develop a better-matched algorithm and a more similar constitutive model to landslides and to apply the numerical simulation method more reasonably.

### 2.1. Dry granular flow

Dry granular flows are the most frequently occurring type of long-runout landslide, including debris and rock avalanches (Perinotto et al., 2015; Deng et al., 2020). The occurrence of debris avalanches has led to the exploration of the possibility that landslides can travel as granular flows without the need for interstitial fluid (Melosh, 1986; Straub, 1996). Dynamic fragmentation often causes an overall volume increase, and the bulking coefficient measures the increase in volume based on the initial and final deposition volumes (Bradley, 1986; Gusman et al., 2009). On June 5, 2009, the catastrophic Jiweishan landslide occurred in Wulong, Chongqing. The sliding main body comprised $500 \times 10^4$ $m^3$ of material, which continuously collided with the surrounding mountain and rapidly disintegrated to form a debris avalanche. This landslide resulted in 74 fatalities (Fig. 1a) (Yin et al., 2011; Gao et al., 2016). On August 28, 2017, an approximately $50 \times 10^4$ $m^3$ landslide produced a debris avalanche and killed 35 people in Nayong and Zhangjiawan, Guizhou Province (Fig. 1b) (Fan et al., 2019).

Please cite this article as: Gao Y et al., Multistate transition and coupled solid–liquid modeling of motion process of long-runout landslide, Journal of Rock Mechanics and Geotechnical Engineering, https://doi.org/10.1016/j.jrmge.2023.12.001

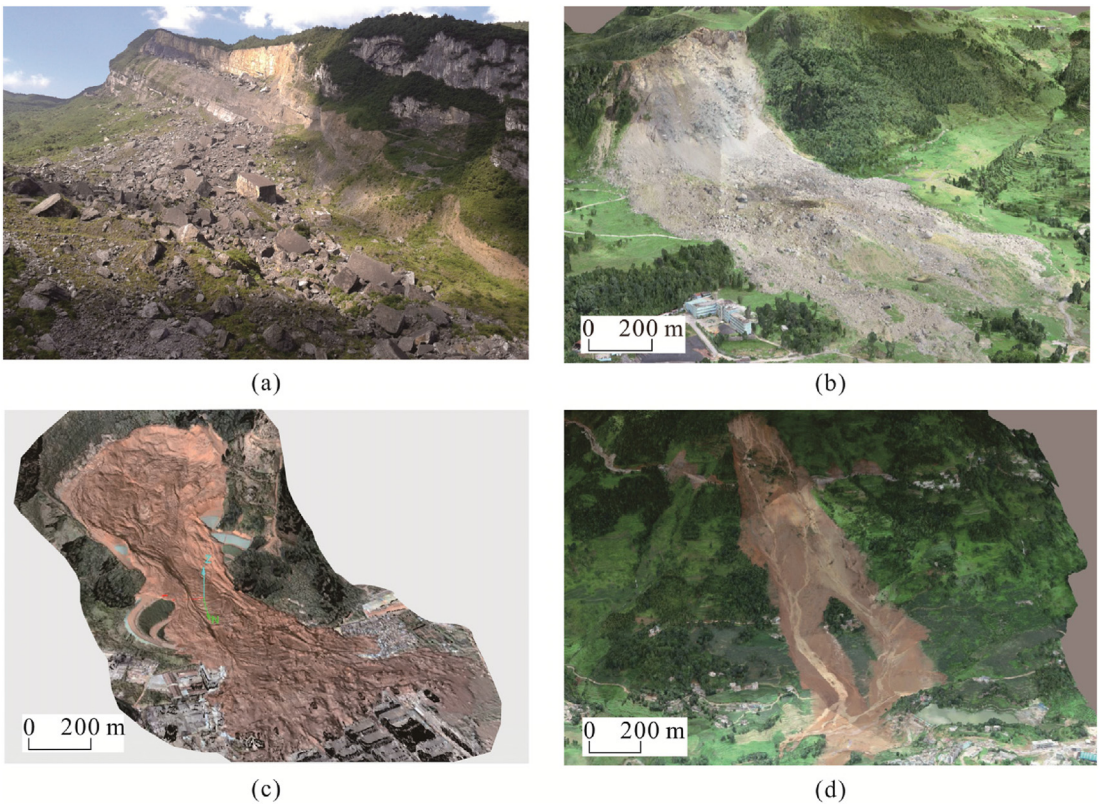


**Fig. 1.** Typical rapid and long-runout landslides in China: (a) Field photo of the Jiweishan landslide in 2009, (b) UAV image of the Zhangjiawan landslide in 2018, (c) UAV image of the Shenzhen "12.20" landslide in 2015, and (d) UAV image of the Shuicheng "7.23" landslide in 2019.

With the development of video and test technology, through repeated observation of videos of past landslides and physical flume models, the grain state and dynamic mode of action during granular debris movement generate steric effects that always vary with the movement position and time (MiDi, 2004; Armanini et al., 2008; Forterre and Pouliquen, 2008; Bryant et al., 2015; Pähtz et al., 2019; Kim and Kamrin, 2020). According to the concentration degree of debris grains, the material state can be mainly divided into dense, dilute and ultradilute states, in which the grains interact by shear, collision and friction, and inertia, respectively, and follow the viscoplastic model, kinetic model of granular flow, and Hertz–Mindlin contact model, respectively. From the perspective of the spatial distribution, the bottom and middle of the granular debris body occur in the dense state, the surface and peripheral margins occur in the dilute state, and discrete rolling particles exhibit the ultradilute state. From the perspective of the temporal process, the initial sliding mass and final accumulation mass mainly occur in the dense state, while the movement process mostly exhibits the dilute state (Fig. 2). The volume fraction is an important indicator to distinguish the different states.

### 2.2. Hyperconcentrated flow

Hyperconcentrated flows occur more frequently in landslides in which the body exhibits a smaller particle size under fully or nearly fully saturated conditions. Hyperconcentrated flow landslide deposits can be distinguished by their longer runout distance, smaller thickness, and smoother surface. Regarding material flows involving small grain size, low bulking factors, and high water content, such as earth, peat and mud flows, the landslide fluidized mobility is higher. Hyperconcentrated flows obey fluid viscous shear models, such as the plastic model and Bingham model (Hutchinson, 1989; Vallance and Scott, 1997). On December 20, 2015, a mudflow occurred in Guangming District, Shenzhen, Guangdong Province, with a volume of $275 \times 10^4$ m$^3$ and an equivalent friction coefficient of only 0.1. This landslide caused 77 fatalities and destroyed 33 houses (Fig. 1c) (Gao et al., 2019).

### 2.3. Mixed flow

Under heavy rainfall and snow and ice melt water, high-flow ground surface runoff can be formed, and a two-phase mixed flow can be generated upon particle mixing. It is therefore necessary to consider the interaction force between the fluid and grain phases. Because landslides can travel longer distances than expected, many researchers have hypothesized that fluids greatly contribute to long-runout landslides (Pudasaini, 2012; Gao et al., 2022). On July 23, 2019, a catastrophic debris flow occurred in Shuicheng, Guizhou Province, China. In this case, basalt debris grain-phase and slurry liquid-phase materials were fully mixed to produce a rapid and long-runout landslide; this debris flow killed 51 people and destroyed and buried 21 houses (Fig. 1d) (Gao et al., 2020). The sliding main body contains two-phase media comprising freely moving fluid and grains, and the fluid is mainly clear water or a slurry composed of water and fine particles. This landslide type mostly includes landslides induced by heavy rainfall and glacial meltwater, and the movement deposition characteristics fall between those of single-phase dry debris grains and fluids (Iverson, 1997; Takarada et al., 1999; Handwerger et al., 2019).

These classifications of long-runout landslides are helpful in numerical algorithm selection. The discrete media algorithm is suitable for dry granular flows, and the continuous media algorithm

Please cite this article as: Gao Y et al., Multistate transition and coupled solid–liquid modeling of motion process of long-runout landslide, Journal of Rock Mechanics and Geotechnical Engineering, https://doi.org/10.1016/j.jrmge.2023.12.001

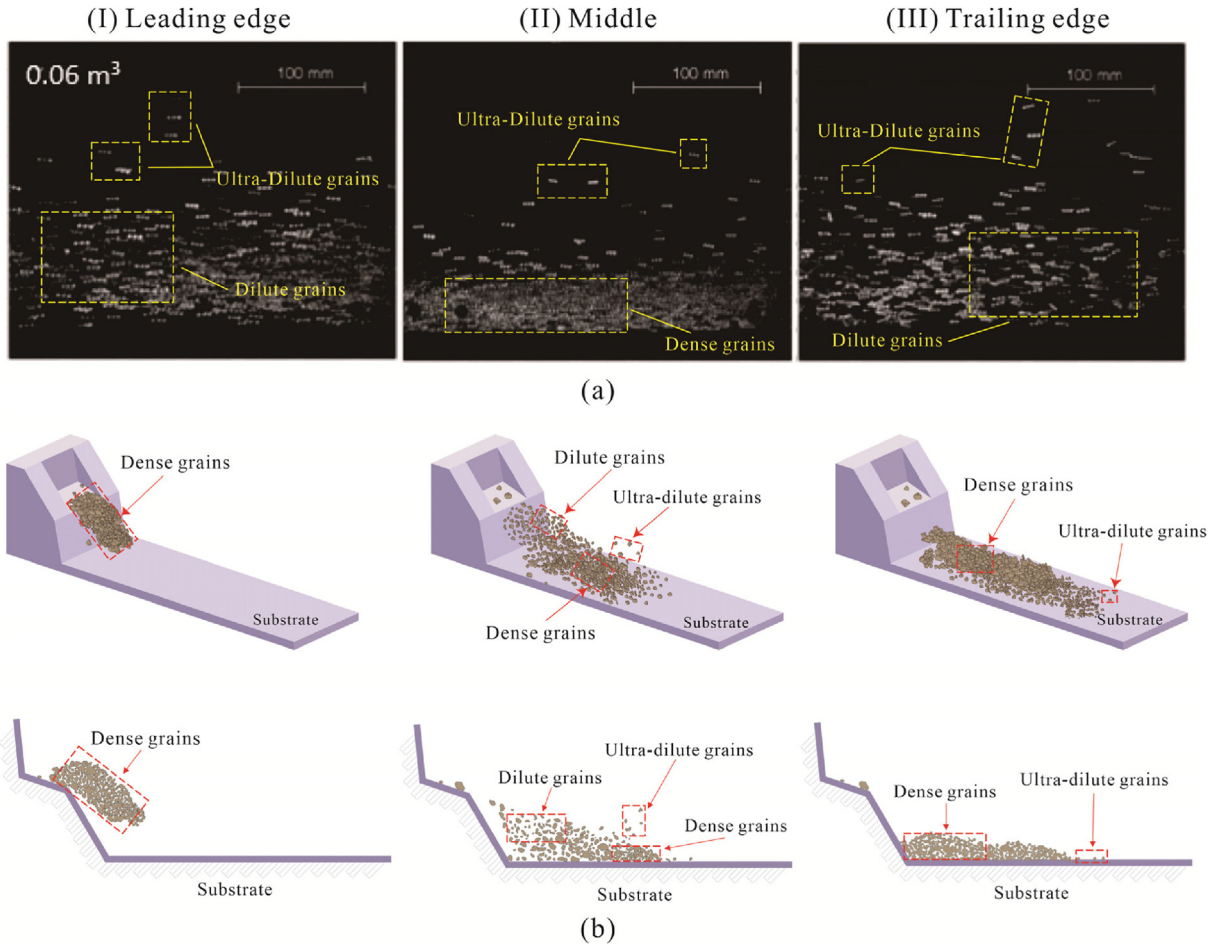


**Fig. 2.** Schematic diagram of the motion state distribution of dry debris grains. Dense grain state of the sliding main body at the post-failure startup stage, dilute grain state and ultradilute grain state of the sliding main body at the rapid mobility stage, and predominant dense state before and after the cessation of clastic body motion: (a) Flume test result (Bryant et al., 2015), and (b) Generalized figure of multistate motion process (Gao et al., 2023; Yin et al., 2023).

can be applied to hyperconcentrated flows. Mixed flows exhibit an intermediate state and are influenced by the coupling between the grain and fluid phases.

## 3. Dynamics algorithm

Based on multistate transition and solid–liquid coupling dynamics modeling, a new numerical simulation method of the LPF$^{3D}$ computing platform was established. This method does not require a mesh and is more computationally efficient than the DEM. The LPF$^{3D}$ method can yield high-efficiency and high-precision solutions of complex dynamic problems under different landslide types, including debris avalanches, mud flows, debris flows, and debris floods.

### 3.1. Governing equation

The governing equations for the materials in the sliding main body in different states are dominated by the principles of mass and momentum conservation given by Eqs. (1) and (2), respectively. In the dilute state, the kinetic model of granular flow can be used as the governing equation, which is the energy equation (Eq. (3)). In this study, the physical units in all equations are international units. The " $=$ " above the symbol denotes a tensor, and the " $\rightarrow$ " above the symbol denotes a vector:

$$\frac{\mathrm{d}\rho}{\mathrm{d}t} = -\rho\frac{\partial\vec{v}}{\partial x} \tag{1}$$

$$\frac{\mathrm{d}\vec{v}}{\mathrm{d}t} = \frac{1}{\rho}\frac{\partial\bar{\bar{\sigma}}}{\partial x} + \vec{f} \tag{2}$$

$$\frac{\mathrm{d}\theta}{\mathrm{d}t} = \frac{2}{3}\left[\frac{\bar{\bar{\sigma}}}{\rho}\frac{\partial\vec{v}}{\partial x} + \frac{\partial}{\partial x}\left(k_{\mathrm{P}}\frac{\partial\theta}{\partial x}\right) - N_{\mathrm{c}}\theta_{\mathrm{P}}\right] \tag{3}$$

where $\rho$ is the material density; $\vec{v}$ is the velocity; $t$ is time; $x$ is the Cartesian component; $\vec{f}$ is the other external forces (e.g., gravitational and interaction forces); and $\mathrm{d}/\mathrm{d}t$ is the total derivative, which describes the conservation relationship of the granular pseudo-temperature $\theta = \langle C^2\rangle/3$ (i.e., the particle's velocity fluctuation); $C$ is the fluctuation velocity of the particles, $k_{\mathrm{P}}\nabla\theta_{\mathrm{P}}$ is the energy dissipation term, $k_{\mathrm{P}}$ is the energy dissipation coefficient, and $N_{\mathrm{c}}\theta_{\mathrm{P}}$ is the energy dissipation term produced by the collisions between discrete grains (Chen and Yan, 2021).

The total stress tensor $\bar{\bar{\sigma}}$ is typically divided into two parts: the isotropic hydrostatic pressure $P$ and the deviatoric friction stress $\tau$. These can be combined as follows:

Please cite this article as: Gao Y et al., Multistate transition and coupled solid–liquid modeling of motion process of long-runout landslide, Journal of Rock Mechanics and Geotechnical Engineering, https://doi.org/10.1016/j.jrmge.2023.12.001

$$\bar{\bar{\sigma}} = -P\delta + \tau \tag{4}$$

where $\delta$ is the Kronecker delta tensor.

The traditional continuum method of SPH can be transformed into the discrete method of SDPH based on the volume fraction and the effective density in a macroscopic continuum algorithm framework. In the SDPH method, grains not only have various physical properties, such as mass, density, velocity, and acceleration but also have various grain properties, such as grain size and volume fraction. Conservation equations were used for the continuous and discrete phases, as described in previous studies (Chen et al., 2017; Cui et al., 2021; Chen and Yan, 2021). The relationship between the profiles of SPH and discrete particles can be obtained with Eq. (5), which can be expressed as follows:

$$\rho_{\mathrm{SPH}} = \rho = \alpha_{\mathrm{p}}\rho_{\mathrm{p}} \tag{5}$$

where $\rho_{\mathrm{SPH}}$, $\alpha_{\mathrm{p}}$, and $\rho_{\mathrm{p}}$ are the density of the SPH fluid, volume fraction and density of the grain phase, respectively.

### 3.2. Constitutive model

Different constitutive models were chosen for the different states in the motion process of a long-runout landslide. The method mainly uses a particle search method with a smoothing radius of 1.3 times the initial grid spacing.

#### 3.2.1. Fluid constitutive model

This constitutive model is mainly adopted for pure aqueous and concentrated fluids. The relationship between the fluid density and pressure $P$ is as follows (Monaghan, 1994):

$$P = P_0\left[\left(\frac{\rho}{\rho_0}\right)^{\gamma} - 1\right] \tag{6}$$

where $P_0 = \rho_0 c_0^2/\gamma$, $\rho_0$ is the initial density of the fluid, $\gamma$ is related to the compressibility of the fluid with $\gamma = 7$, and $c_0$ is the initial velocity of sound (to ensure the compressibility of the fluid, it is generally assumed that $c_0 = 10v_{\max} \sim 40v_{\max}$, where $v_{\max}$ is the maximum velocity of the fluid).

For a Newtonian fluid, the viscous friction stress $\tau$ (Eq. (7)) is proportional to the friction strain rate $\varepsilon$ (Eq. (8)), and the scaling coefficient is the viscosity coefficient $\mu$. For a non-Newtonian fluid, $\mu$ is a function of the friction strain rate:

$$\tau = \mu\varepsilon \tag{7}$$

$$\varepsilon = \nabla \bullet \vec{v} + \nabla \bullet \vec{v}^{\mathrm{T}} - \frac{2}{3}(\nabla \bullet \vec{v})\delta \tag{8}$$

where $\nabla \bullet \vec{v}$ is the divergence of velocity, and the other parameters are the same as those in Eq. (3).

#### 3.2.2. Dense state of grains–viscoplastic constitutive model

The hydrostatic pressure can be directly calculated from the granular constitutive equation using the standard definition of the mean stress as follows:

$$P = -\frac{1}{3}(\sigma^{xx} + \sigma^{yy} + \sigma^{zz}) \tag{9}$$

where $\sigma^{xx}$, $\sigma^{yy}$, and $\sigma^{zz}$ are the components of the stress tensor along the $x$, $y$, and $z$ directions, respectively. In a quasistatic state, the particles mainly generate elastic deformation. At this stage, the stress–strain relationship of the particles can be obtained according to Hooke's law:

$$\dot{\sigma} = 2G\dot{e} + K\dot{\varepsilon}\delta \tag{10}$$

where $\dot{\sigma}$ is the incremental form of the stress component, $G$ is the friction modulus ($G = \frac{E}{[2(1+v)]}$), $K$ is the elastic modulus ($K = \frac{E}{[3(1-2v)]}$), $E$ is Young's modulus, and $\dot{e} = \dot{\varepsilon} - \frac{\dot{\varepsilon}^{kk}\delta}{3}$ is the deviatoric friction strain rate tensor (strain rate tensor: $\dot{\varepsilon} = \frac{1}{2}(\nabla \bullet \vec{v} + \nabla \bullet \vec{v}^{\mathrm{T}})$):

$$\tau = \frac{\mu(I)P}{|\dot{\varepsilon}|}\varepsilon \tag{11}$$

where $\tau$ is the deviatoric stress component, $|\dot{\varepsilon}|$ is the second invariant, and $\varepsilon$ is the strain rate tensor, which can be defined according to the law of the friction coefficient $\mu(I)$. This also suggests that the volume fraction monotonically depends on the inertia constant:

$$\mu(I) = \mu_{\mathrm{P}} + \frac{(\mu_2 - \mu_{\mathrm{P}})}{\left(\frac{I_0}{I} + 1\right)} \tag{12}$$

In this study, experiments and numerical simulations were conducted, and it was found that in the function $\mu(I)$, the minimum value $\mu_{\mathrm{p}}$ for a very low inertia constant $I$ (quasistatic) gradually increased to a finite value $\mu_2$ with increasing $I$ value. $I_0$ is a constant, and the parameters in the equation depend on the material properties. For example, typical values are $\mu_{\mathrm{p}} = \tan 21^{\circ}$, $\mu_2 = \tan 33^{\circ}$, and $I_0 = 0.28$ (MiDi, 2004).

$$I = \frac{|\dot{\varepsilon}|d_{\mathrm{P}}}{\left(\frac{P}{\rho_{\mathrm{p}}}\right)^{0.5}} \tag{13}$$

where the inertia constant is the ratio between the macroscopic deformation time scale ($1/|\dot{\varepsilon}|$) and the inertial time scale $(d_{\mathrm{p}}{}^2\rho_{\mathrm{p}}/P)^{0.5}$, in which $d_{\mathrm{p}}$ is the particle size, and $\rho_{\mathrm{p}}$ is the particle density.

#### 3.2.3. Dilute state of grain–kinetic modeling of the granular flow constitutive model

In particle dynamics modeling, the sliding main body refers to a macroscopic continuum comprising particles. The normal stress $P$ includes collision and kinetic pressure, which can be obtained as follows:

$$P = \rho[1 + 2(1+e)\alpha_{\mathrm{p}}g_0]\theta \tag{14}$$

where $\alpha_{\mathrm{p}}$ is the volume fraction of particles and $g_0$ is the collision recovery coefficient of the particles, which can be calculated as follows:

$$g_0 = \left[1 - \left(\frac{\alpha_{\mathrm{p}}}{\alpha_{\mathrm{p,max}}}\right)^{\frac{1}{3}}\right]^{-1} \tag{15}$$

where $\alpha_{\mathrm{p,max}}$ is the maximum volume fraction of the granular material under compressible conditions.

Please cite this article as: Gao Y et al., Multistate transition and coupled solid–liquid modeling of motion process of long-runout landslide, Journal of Rock Mechanics and Geotechnical Engineering, https://doi.org/10.1016/j.jrmge.2023.12.001

$$\theta = \frac{1}{3}(v - \bar{v})^2 \tag{16}$$

where $v$ is the particle instantaneous velocity and $\bar{v}$ is the particle average velocity.

The friction stress $\tau$ can be calculated as follows:

$$\begin{aligned}\overline{\overline{\tau}} = & \frac{4\alpha_p^2\rho_p d_p g_0(1+e_{PP})}{3}\sqrt{\frac{\theta_P}{\pi}}\nabla \bullet \overrightarrow{v} \\ & + 2\left[\frac{4\alpha_p^2\rho_p d_p g_0(1+e_{PP})}{5}\sqrt{\frac{\theta_P}{\pi}}\right. \\ & \left. + \frac{2\frac{5\sqrt{\pi}}{96}\rho_p d_p\sqrt{\theta_P}}{g_0(1+e_{PP})}\left(1+\frac{4}{5}\alpha_p g_0(1+e_{PP})\right)^2\right]\end{aligned} \tag{17}$$

where $e_{PP}$ is the collision recovery coefficient, representing the energy loss during the collision and is equal to 1 in a completely elastic collision.

### 3.2.4. Ultradilute state of the grain-Hertz–Mindlin contact model

The DEM can be separately described by Newton's second law, which can be expressed as follows:

$$m_i\frac{dv_i}{dt} = \sum_{j=1}^{k_i}\left(F_{c,ij} + F_{d,ij}\right) + m_i g \tag{18}$$

where $m_i$ and $v_i$ are the mass and velocity of particle $i$, respectively, $m_i g$ is the particle gravity, $F_{c,ij}$ and $F_{d,ij}$ are the contact and viscous contact damping forces, respectively, between particles $i$ and $j$, and $k_i$ is the total number of particles in contact with another particle. The contact force between particles $i$ and $j$ can be divided into normal and friction contact forces. The contact model is the Hertz–Mindlin model.

The normal force $F_{Hertz}$ can be calculated as follows:

$$F_{Hertz} = k_n\delta_n \tag{19}$$

where $\delta_n$ is the overlap of particles at the contact; and $k_n = \frac{4}{3}E^*\sqrt{R^*\delta_n}$, is the normal stiffness, and this equation illustrates that the model is nonlinear and elastic, in which $E^*$ is the equivalent Young's modulus ($\frac{1}{E^*} = \frac{1}{E_i} + \frac{1}{E_j}$, where $E_i$ and $E_i$ are the Young's moduli of two impact particles), and $R^*$ is the equivalent radius ($\frac{1}{R^*} = \frac{1}{R_i} + \frac{1}{R_j}$, where $R_i$ and $R_j$ are the contact radii of two impact particles).

The friction contact force $F_{Mindlin}$ is a function of the friction overlap $\delta_t$:

$$F_{Mindlin} = k_t\delta_t \tag{20}$$

where $k_t = 8G^*\sqrt{R^*\delta_t}$ is the friction stiffness and $G^*$ is the equivalent friction modulus ($\frac{1}{G^*} = \frac{1}{G_i} + \frac{1}{G_j}$).

Collisions between particles are often accompanied by energy loss, and the normal and friction damping forces can be expressed as follows:

$$F_n^d = -2\sqrt{\frac{5}{6}}\beta\sqrt{k_n m^*}v_n\overrightarrow{rel} \tag{21}$$

$$F_t^d = -2\sqrt{\frac{5}{6}}\beta\sqrt{k_t m^*}v_t\overrightarrow{rel} \tag{22}$$

where $\beta = \frac{\ln e}{\sqrt{\ln^2 e_{PP} + \pi^2}}$, and $v_n\overrightarrow{rel}$ and $v_t\overrightarrow{rel}$ are the normal and friction components of the relative velocity, respectively.

## 3.3. Transition and coupling

### 3.3.1. Dense grain–dilute grain transition

The transitional regime remains poorly understood, and the extent to which the simulation results are applicable to real granular systems is unknown. In simulations of debris avalanches, the volume fraction and constitutive model have been used to obtain solutions for the different states of the sliding main body. There are four motion states of the sliding main body: dense grains, transition between dense and dilute grains, dilute grains, and ultradilute grains. Their constitutive models are the viscoplastic constitutive model, kinetic model of granular flow, and DEM constitutive model (Fig. 3).

When using the algorithm for translation of the dense grain state into the dilute grain state, the physical parameters of the particles should initially remain unchanged, and the main difference lies in the interaction force between the particles. The elastic normal stress of a dense grain flow translates into the frictional normal stress of a dilute grain flow:

$$P = P_{friction} = Fr\frac{(\alpha_p - \alpha_{p,min})^n}{(\alpha_{p,max} - \alpha_p)^m} \tag{23}$$

Where $P_{friction}$ is the normal friction stress. $Fr$, $n$, and $m$ are empirically determined material constants of 0.5, 2, and 5, respectively (Johnson et al., 1990). The normal stress value can be obtained by friction according to the change in the volume fraction $\alpha_P$. The tangential stress $\tau$ can be calculated using Eq. (11). At the beginning of the transition process, the pseudo-temperature is calculated from zero, and the normal and friction stresses generated by the collision gradually increase until the entire transition zone is transformed into the particle dynamics model.

### 3.3.2. Dilute grain–dense grain transition

In the transition from the dilute grain state to the dense grain state, the physical parameters of the particles also remain unchanged, and the main difference lies in the interaction force between the particles. The pseudo-temperature of the dilute grains decreases from the transition zone, and the collision stress gradually decreases. However, the frictional normal stress $P_{friction}$ gradually increases, and the friction increases. The rheological friction stress equation was used in the simulations until the dilute grain state was transformed into the dense grain state. At this time, with decreasing friction force, the elastic friction force gradually increased, the particle velocity gradually decreased, and the volume fraction gradually increased until a quasistatic state was reached.

### 3.3.3. Dense grain–dilute grain interaction

When dense and dilute grain flows occur concurrently, interaction ensues between the particles in these two states. When the particles in these two states are adjacent, it is necessary to determine their involvement in the simulation of the stress and velocity with respect to each other. When the dilute grains are active particles and the dense grains are passive particles, the dense grains

Please cite this article as: Gao Y et al., Multistate transition and coupled solid–liquid modeling of motion process of long-runout landslide, Journal of Rock Mechanics and Geotechnical Engineering, https://doi.org/10.1016/j.jrmge.2023.12.001

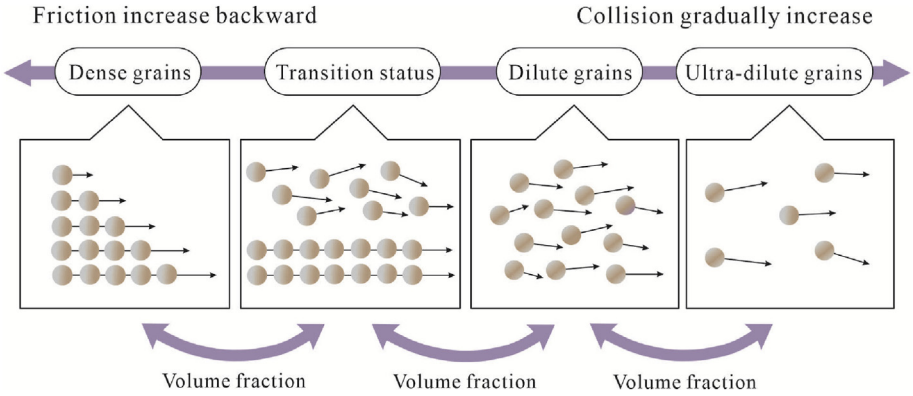


**Fig. 3.** Schematic diagram showing the transition of the state of the grains. During motion, the sliding main body can be classified into dense, dilute, and ultradilute states, and the volume fraction is used as a criterion to discriminate the grain state.

participate in the simulation of the velocity gradient of the dilute grains. Conversely, when the dense grains are active particles and the dilute grains are passive particles, the dilute grains do not participate in the simulation of the velocity gradient of the dense grains.

#### 3.3.4. Two-phase coupling

The continuous fluid phase and discrete solid phase were simulated using the SPH and SDPH methods, respectively. Interphase forces play a key role in the coupling between the continuous fluid phase and the discrete solid phase. The interaction between these two phases is also driven by the drag force of another phase. Therefore, the grain phase interacts with the continuous phase, affecting its internal force, and the exchanged interactions produce the drag force and pressure. The time step of the coupling method is determined by the minimum time step between the SPH and SDPH methods.

The drag force per unit mass $\vec{R}_{\mathrm{fp}}$ can be expressed as follows:

$$\vec{R}_{\mathrm{fp}} = \frac{\beta_{\mathrm{fp}}\left(\vec{v}_{\mathrm{f}} - \vec{v}_{\mathrm{p}}\right)}{\alpha_{\mathrm{p}}\rho_{\mathrm{p}}} \tag{24}$$

where $\vec{v}_{\mathrm{f}}$ and $\vec{v}_{\mathrm{p}}$ are the solid and fluid velocities, respectively.

The interaction between particles and fluid in two-phase flow proposed by Gidaspow (1994) was specifically used in this study. The Ergun equation was used for dense phase simulation purposes, and the Wen-Yu equation was used for dilute phase simulation purposes (Ergun, 1952; Wen and Yu, 1966):

Here, the momentum transfer coefficient between the fluid and solid $\beta$ can be defined as follows:

$$\beta_{\mathrm{fp}} = \left(1 - \varphi_{\mathrm{fp}}\right)\beta_{\mathrm{Ergun}} + \varphi_{\mathrm{fp}}\beta_{\mathrm{Wen-Yu}} \tag{25}$$

$$\beta = \begin{cases} \beta_{\mathrm{Ergun}} = 150\dfrac{\alpha_{\mathrm{p}}^2\mu_{\mathrm{f}}}{\alpha_{\mathrm{f}}d_{\mathrm{p}}^2} + 1.75\dfrac{\alpha_{\mathrm{p}}\rho_{\mathrm{f}}}{d_{\mathrm{p}}}\left|\vec{v}_{\mathrm{f}} - \vec{v}_{\mathrm{p}}\right|, \alpha_{\mathrm{f}} < 0.8 \\ \beta_{\mathrm{Wen-Yu}} = \dfrac{3}{4}C_D\dfrac{\alpha_{\mathrm{p}}\alpha_{\mathrm{f}}\rho_{\mathrm{f}}}{d_{\mathrm{p}}}\left|\vec{v}_{\mathrm{f}} - \vec{v}_{\mathrm{p}}\right|\alpha_{\mathrm{f}}^{-2.65}, \alpha_{\mathrm{f}} \geq 0.8 \end{cases} \tag{26}$$

where $\beta_{\mathrm{Ergun}}$ and $\beta_{\mathrm{Wen-Yu}}$ respectively denote the momentum transfer coefficients defined by Ergun and Wen-Yu, $C_D$ is the drag force coefficient, $\mu_{\mathrm{f}}$ is the fluid viscosity,

To eliminate the discontinuity between these two equations, a relaxation factor was introduced to smooth the momentum exchange coefficient in the transition region:

$$\varphi_{\mathrm{fp}} = \frac{\arctan\left[150 \times 1.75\left(0.2 - \alpha_{\mathrm{p}}\right)\right]}{\pi} + 0.5 \tag{27}$$

$C_D$ can be defined as follows:

$$C_D = \begin{cases} \dfrac{24}{\alpha_{\mathrm{f}}Re_{\mathrm{P}}}\left[1 + 0.15\left(\alpha_f Re_P\right)^{0.687}\right], Re_{\mathrm{P}} < 1,000 \\ 0.44, Re_{\mathrm{P}} \geq 1,000 \end{cases} \tag{28}$$

The relative Reynolds number $Re_{\mathrm{P}}$ can be defined as follows:

$$Re_{\mathrm{P}} = \frac{\rho_{\mathrm{f}}d_{\mathrm{p}}\left|\vec{v}_{\mathrm{f}} - \vec{v}_{\mathrm{p}}\right|}{\mu_{\mathrm{f}}} \tag{29}$$

### 3.4. Basal boundary force

Boundary forces were applied using the penalty function method, and the forces between the grains and boundary were decomposed into a normal force $\vec{f}^{n}$ and a tangential force $\vec{f}^{\tau}$. The boundary normal force is applied to the penalty function formula, in which the repulsive force is directly applied to the boundary particles. The penalty parameter was modified to make it proportional to the distance and velocity between the particles and the boundary. The boundary tangential force was selected according to the material properties of the sliding body, and different resistance models were used for the fluid and the solid.

Regarding the normal force, the contact condition was defined using the penalty function method (Qiang et al., 2011) as follows:

Please cite this article as: Gao Y et al., Multistate transition and coupled solid–liquid modeling of motion process of long-runout landslide, Journal of Rock Mechanics and Geotechnical Engineering, https://doi.org/10.1016/j.jrmge.2023.12.001

$$\vec{f}^{\,n} = \begin{cases} -\omega 2h_i \sum\limits_{j\in B}\left(\dfrac{1}{\left|\vec{r}_{ij}\right|}\left(\vec{v}_i - \vec{v}_j^{\,B}\right)\cdot\vec{n}_j W_{ij}A_j\vec{n}_j\right) & \left(\vec{v}_i - \vec{v}_j^{\,B}\right)\cdot\vec{n}_j < 0 \\ 0 & \left(\vec{v}_i - \vec{v}_j^{\,B}\right)\cdot\vec{n}_j \geq 0 \end{cases} \tag{30}$$

where $\omega$ is the penalty parameter, $\vec{r}_{ij}$ is the radial vector between grains $i$ and $j$, $\vec{v}_i$ is the velocity vector of grain $i$, $\vec{v}_j^{\,B}$ is the velocity vector of boundary grain $j$, $\vec{n}_j$ is the normal vector of boundary grain $j$, $W_{ij}$ is the kernel function between grains $i$ and $j$, and $A_j$ is the area of boundary grain $j$.The repulsive force is directly applied on the boundary particles. The penalty parameter was modified to make it proportional to the distance and velocity between the particles and the boundary (Li and Liu, 2002).

The tangential substrate resistance force between the sliding main body and the boundary layer was selected according to the material properties of the sliding body, and different resistance models were used for the fluid and grains (Hungr et al., 2001, 2002).

The frictional model of the solid can be expressed as follows:

$$\vec{f}^{\,\tau} = \sigma(1 - r_u)\tan\Phi \tag{31}$$

where $\sigma$ is a function of only the total normal stress at the bottom, $r_u$ is the pore pressure coefficient, and $\Phi$ is the friction angle.

The laminar model of a fluid can be expressed as follows:

$$\vec{f}^{\,\tau} = \frac{3v\mu}{H} \tag{32}$$

where $\mu$ is the dynamic viscosity coefficient, $v$ is the velocity of the fluid, and $H$ is the fluid depth.

## 4. Flume experiment validation

To ensure the applicability of the numerical models at different scales, small-scale experiments were performed to validate the multistate transition modeling results for dry grain material and coupling modeling results for mixed solid–liquid material.

### 4.1. Experimental design

In this study, a flume test was conducted to verify the dynamic modeling and algorithm numerical parameters. The experimental setup consisted of a hopper in the sliding source area, a flume in the circulation area, and a bottom plate in the accumulation area. The size of the experimental equipment is designed mainly considering the influence of the site, and the sample is selected mainly considering the operability. The size of the flume was 3 m × 0.5 m × 0.5 m with an inclination angle of 20°, and the size of the hopper was 0.5 m × 0.5 m × 0.5 m. The hopper was watertight and was used to prepare and store the initial sliding body material. Transparent glass on both sides of the flume was used to observe the movement of the sliding main body and to measure the thickness. The size of the bottom plate was 2.4 m × 4.8 m (Fig. 4). The solid material used to simulate the sliding body in this flume experiment was limestone crushed gravel. First, a certain amount of limestone was obtained on site and crushed into gravel-sized particles, after which the gravel particles were sieved to a 10–30 mm grain size. The slurry was a viscous fluid with a density of 1570 kg/m$^3$ comprising fine-grained soil (clay with a particle size ranging from 0.005 to 0.05 mm) and water. Specific sliding main bodies were prepared for the different conditions by mixing gravel particles with mud and water (Table 1). The test was mainly designed to capture three working conditions: (I) dry grains; (II) dry grains mixed with a 30% slurry by volume; and (III) dry grains mixed with a 70% slurry by volume. The multistate transition and solid–liquid coupling dynamics model and parameters were each validated via three sets of trials. The sliding main body slides along the flume, assuming that the effect of the complex terrain on its movement is not accounted for. During the testing process, it is necessary to control the mixing ratio of the landslide material and slurry to ensure the comparability of the experiments and the accuracy of the results.

### 4.2. Numerical model and parameter selection

The parameters of the materials used in the simulation were consistent with those in the flume test (Tables 1 and 2). Under working condition I, multistate transition theory was used to simulate the motion process of dry grains. The critical volume fractions of particles in the dense, dilute and ultradilute states were 60% and 2%, respectively. Regarding the selection of the critical volume fraction value, some literature uses several physical and numerical experiments to compare and verify that friction and collision are the main action modes affecting the motion state of the sliding main body. The set volume fraction is used as the critical value of the interval range, and then the critical volume fraction is employed to discriminate the state of the grains, i.e., which of the dense, transitional, dilute, and ultradilute states it belongs to. When the collision effect is smaller and the friction-dominated volume fraction of dense-state particles is more than 50%–60%, the macromechanical constitutive is obeyed. When the friction effect is smaller, the dilute state dry debris body dominated by the collision effect is suitable for the kinetic theory of granular flow (KTGF) calculation, with a particle volume fraction of smaller than 50%–60%. In the ultradilute state, when a particle volume fraction is smaller than 2%, the grains obey Newton's second law without considering particle–particle interactions, realizing the minimum number of grains to achieve high computational efficiency (Mezhericher et al., 2011). Under working conditions II and III, a solid–liquid coupling model was used to simulate the motion process of the sliding main body with different volume fractions of mixed slurry and grains. The initial volume fractions of liquid were 30% and 70%, and the sum of the volume fractions at the location of solid and liquid mixing was 1.

The friction coefficient and pore pressure coefficient are important parameters that affect the basal tangential force (Larcher et al., 2007; Pudasaini and Miller, 2013). In the numerical simulation process, the trial and error method was used to determine the friction coefficient at the boundary between the flume and sliding body material under working condition I. The pore pressure at the

Please cite this article as: Gao Y et al., Multistate transition and coupled solid–liquid modeling of motion process of long-runout landslide, Journal of Rock Mechanics and Geotechnical Engineering, https://doi.org/10.1016/j.jrmge.2023.12.001

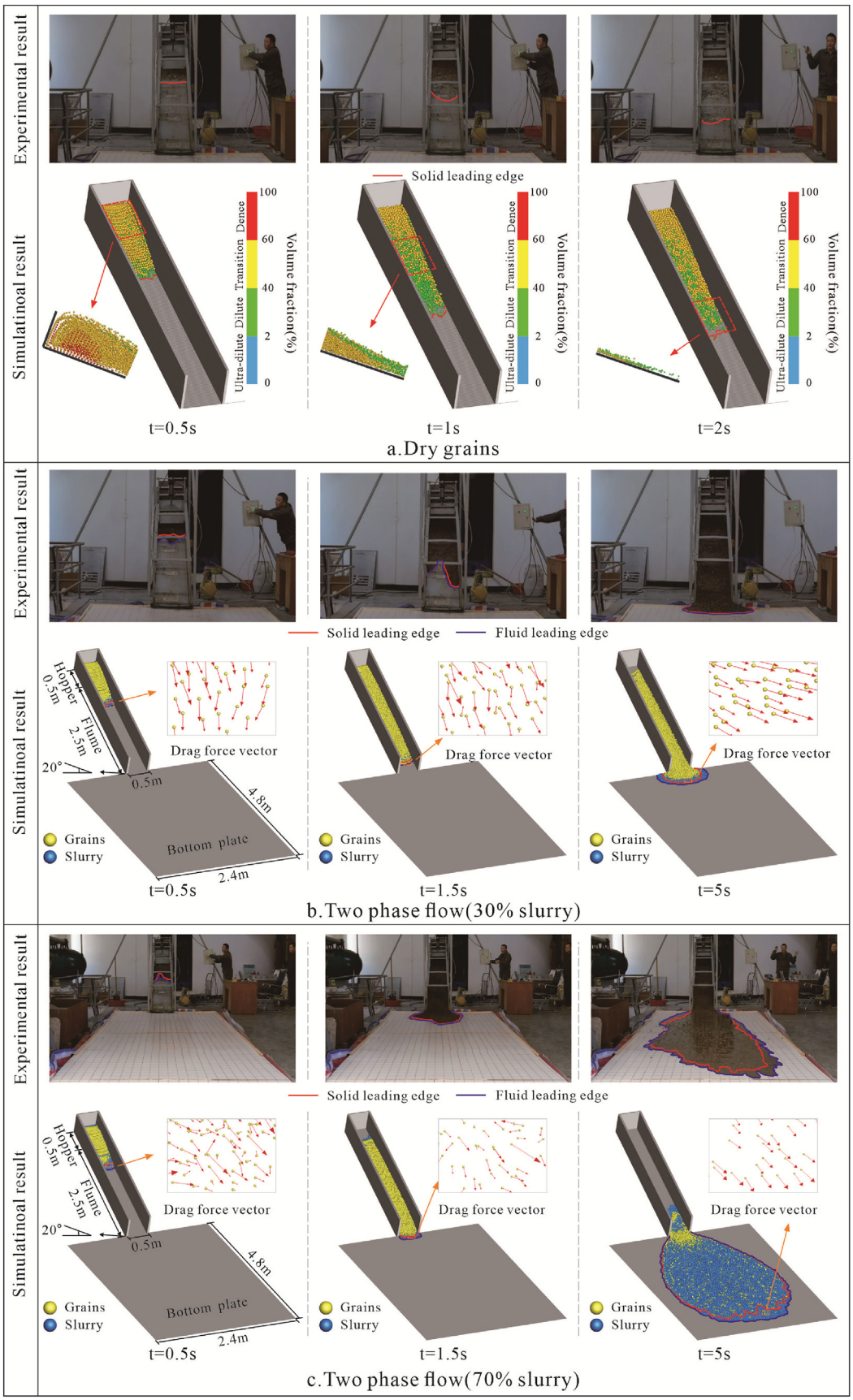


**Fig. 4.** Experimental and simulation results of the three working conditions of the flume experiment, including the grain state at different moments and the vector of fluid drag force on solid grains at different moments: (a) Dry grains, (b) Two phase flow (30% slurry), and (c) Two phase flow (70% slurry).

Please cite this article as: Gao Y et al., Multistate transition and coupled solid–liquid modeling of motion process of long-runout landslide, Journal of Rock Mechanics and Geotechnical Engineering, https://doi.org/10.1016/j.jrmge.2023.12.001

basal boundary varied at different locations. After analysis of the relevant literature, it was concluded that the pore pressure coefficient for a flume model of the same size varies between 0.4 and 0.8 (Reid et al., 2008; Iverson et al., 2010; Kaitna et al., 2016; Zhou et al., 2019). In our study, several back-simulations were performed to determine the pore pressure parameters in the boundary resistance model, with the employed parameters presented in Table 2.

### 4.3. Result analysis

#### 4.3.1. Motion process

Fig. 4 shows a comparison of the simulated motion process between the three working conditions and the test at different moments. In the posttreatment, different particles in yellow and blue were used to represent solid grains and fluid, respectively. The leading edges of the yellow and blue particles are the leading edges of the solid and fluid. Under condition I, most of the dry grains remained in the flume, and a small number of gravel grains were discharged from the flume and stopped at the bottom plate. Fig. 4a shows the change in the volume fraction during the movement of dry grains in the numerical simulation process. The results captured the distribution of particles in the dense, transition and dilute states at the different motion stages and positions. Under condition II, the 30% slurry mostly occurred in a state of integral motion and eventually produced a fan-shaped accumulation at the bottom plate. Vector diagrams of the interphase forces showed clear solid–liquid interactions of the drag force (Fig. 4b). Under condition III, when the 70% slurry occurred in a state of overall movement and the grains were uniformly distributed between the flume and at the bottom plate, the liquid imposed a drag effect on the solid grains (Fig. 4c). In summary, the numerical simulation results from initiation to final material accumulation better simulated the motion process of dry granular flows and solid–liquid two-phase flows, and the motion process was highly consistent with the experimental process.

Fig. 5 shows a comparison of the experimental and simulation accumulation results and the velocity profiles of the leading grains. The yellow line denotes the accumulation results for dry grains, the blue line indicates the fluid accumulation results, the solid line denotes the experimental results, and the dashed line indicates the numerical simulation results. Under condition I, except for a small number of grains that moved to the bottom plate, most grains were evenly distributed in the flume, and the distance traveled reached approximately 2.7 m. Moreover, the movement velocity initially increased and then decreased, with a maximum velocity of 2.3 m/s, which is essentially the same as the maximum test velocity. Under condition II, in both the simulation and experiment, the grains were evenly distributed in the flume and at the exit of the flume, and the accumulation pattern resembled a fan. The distance traveled was approximately 3.7 m, and the maximum velocity reached 1.7 m/s, which is very similar to the maximum test velocity. Under condition III, the accumulation state of grains in the simulation and experiment were similar to those under condition II, but the simulation result was closer to ideal, with a symmetrical accumulation pattern and a distance traveled of approximately 7.7 m. The maximum velocity was 3.7 m/s, which is very similar to the maximum test velocity.

#### 4.3.2. Accumulation shape and velocity

Considering the numerical simulation results of the motion process, accumulation range, velocity curve, and the numerical results were generally consistent with the experimental results. The applicability of the multistate transition and solid–liquid coupling dynamics modeling was verified. In the numerical flume experiment, the algorithm parameters were assessed (the imaginary sound speed, artificial viscosity, and artificial stress) to achieve the optimal simulation results. By comparing the selected microscopic parameters of grains (grain quantity and contact parameters), this numerical method could efficiently and realistically simulate the landslide post-failure process based on realistic physical and mechanical parameters.

## 5. Case studies

Through the physical model and numerical simulation of the flume test, LPF$^{3D}$ can be employed to suitably reduce and analyze small-scale cases based on multistate transition and solid–liquid coupling theory. To verify the effectiveness and applicability of LPF$^{3D}$ based on realistic landslide and field data, two cases (Zhangjiawan debris avalanche and Shuicheng debris flow) were simulated and analyzed.

### 5.1. Case study of the Zhangjiawan landslide

On August 28, 2017, a large-scale mountain rock avalanche occurred in Nayong County, Guizhou Province, China. The rock mass with a volume of $49.1 \times 10^4$ m$^3$ moved down and scraped the original loose deposits and finally formed deposits of $82.3 \times 10^4$ m$^3$, which destroyed parts of Pusa village, resulting in 35 deaths (Fan et al., 2019). After the mountain was destabilized, the sliding main body was rapidly broken, disintegrated, and moved at high speed. Along the way, it scraped the original loose material on the slope surface, and the volume continued to increase until the movement was blocked by the buildings in Pusa village. In the motion process, the landslide eventually generated deposition bodies, with an average thickness of 4 m, a longitudinal length of approximately 840 m, and a total volume of approximately $82.3 \times 10^4$ m$^3$.

Terrain and landslide models were created using 1:2000 contour data. According to the field survey results, the volume of the sliding main body was $49.1 \times 10^4$ m$^3$. The average grain size was approximately 3 m. The critical values for the critical volume fractions of particles in the different states were set to 60% and 2%. The height difference (H) between the trailing edge and front edges is approximately 305 m, and the maximum displacement distance (L) reaches 840 m, with an equivalent coefficient friction of approximately 0.3. The value was determined based on the equivalent friction coefficient in this study. The physical and mechanical parameters of the landslide materials used are provided in Table 3.

Fig. 7 shows the post-failure motion process based on initial startup, potential/kinetic energy conversion, and final deposition. The red dotted line in Fig. 7a indicates the landslide deposition range. The maximum velocity of individual particles at the front edge of the landslide was 21 m/s, and the overall average maximum velocity of the landslide was approximately 12 m/s. The maximum horizontal movement distance was 830 m, which is 10% less than the actual landslide. The maximum deposition thickness was

**Table 1**
Material parameters for the flume experiment.

| Parameters | Limestone grain | Slurry |
|---|---|---|
| Density (kg/m$^3$) | 2600 | 1570 |
| Viscosity coefficient (Pa•s) | 1570 | 0.018 |
| Quality (kg) | 100 | 0/36.3/84.5 |
| Grain size (m) | 0.02 | – |
| Elastic modulus (MPa) | $5 \times 10^4$ | – |
| Poisson's ratio | 0.28 | – |
| Internal friction angle (°) | 20 | – |

Please cite this article as: Gao Y et al., Multistate transition and coupled solid–liquid modeling of motion process of long-runout landslide, Journal of Rock Mechanics and Geotechnical Engineering, https://doi.org/10.1016/j.jrmge.2023.12.001

**Table 2**
Numerical simulation parameters of LPF$^{3D}$ for the flume experiment.

| Parameters | Working condition-I | Working condition-II | Working condition-III |
|---|---|---|---|
| Friction coefficient (Limestone grain) | 0.8 | 0.8 | 0.8 |
| Pore pressure coefficient (Flume) | 0 | 0.5 | 0.5 |
| Pore pressure coefficient (Bottom plate) | 0 | 0.6 | 0.85 |
| Fluid volume fraction (%) | – | 30 | 70 |

12.7 m behind the hillslope. The deposition features were the same as those of the landslide (Fig. 7b).

Fig. 7c shows the distribution of the SPH particle volume fraction during landslide movement. The dense state is shown in red, yellow indicates the transition state from the dense to dilute states, green indicates the dilute state, and blue denotes the ultradilute state. The initial volume fraction of the sliding main body grains was set to 70%. In the simulation process, the SPH particle mass remained constant and equal to the total mass of the particle group. When the particle volume fraction decreased, the particle size accordingly increased. The SPH particles are shown in different colors based on the particle state or volume fraction (Fig. 7c). The change in the volume fraction distribution in the tail landslide movement process showed that the slide occurred in the dense state at the initial stage after landslide instability, and the grains gradually transitioned to the dilute state in the acceleration process. When the sliding main body impacted the surrounding stable mountains, the collision led to an increase in the grain velocity followed by another decrease in the volume fraction. After the Zhangjiawan landslide disintegrated and moved down, the grains did not present an ultradilute state because the terrain it passed through was relatively flat and the sliding main body did not exhibit very intense movement. At the final accumulation stop stage, most of the bottom grains of the accumulation body returned to the dense state. The simulation results based on multistate transition and solid–liquid coupling dynamics modeling were generally consistent with the physical and mechanical motion characteristics of a debris avalanche.

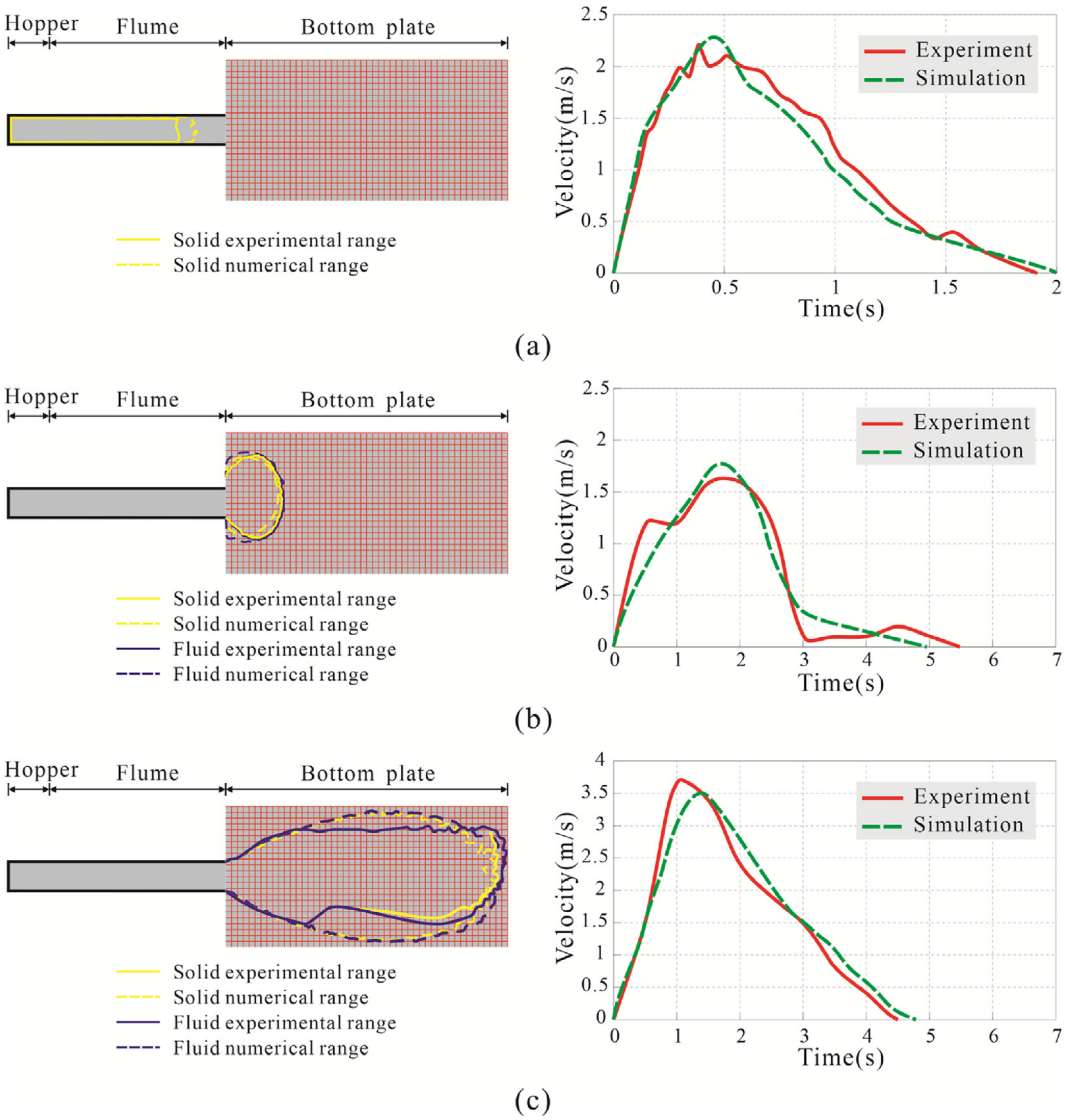


**Fig. 5.** Comparison of the experimental and simulation accumulation results and velocity profiles of the leading grains. The accumulation comparison profile is located on the left, and the velocity comparison profile is on the right: (a) Dry grains, (b) Two phase flow (30% slurry), and (c) Two phase flow (70% slurry).

Please cite this article as: Gao Y et al., Multistate transition and coupled solid–liquid modeling of motion process of long-runout landslide, Journal of Rock Mechanics and Geotechnical Engineering, https://doi.org/10.1016/j.jrmge.2023.12.001

**Table 3**
LPF$^{3D}$ simulation parameters for the Zhangjiawan landslide.

| Parameters | Value |
|---|---|
| Density (kg/m$^3$) | 2400 |
| Cohesion (kPa) | 5 |
| Internal friction angle (°) | 24 |
| Friction coefficient | 0.24 |
| Grain diameter(m) | 3 |
| Numerical particle number | 51897 |
| Debris grain number | 24324 |
| Dense/dilute/ultradilute critical volume fraction (%) | 60/2 |

According to measured section M-M' (Fig. 8), the simulation results matched the landslide deposition features (Fig. 6). Monitoring points were set at horizontal distances of 190 m, 340 m and 685 m in the section depicted in Fig. 10 to illustrate the changes in the motion velocity during the conversion of the potential kinetic energy. Based on the monitoring data, the sliding main body grains showed an overall trend of rising and then decreasing for a short period. After crossing the hillslope, the grains located at the rear continued to transfer energy to the grains at the front, resulting in a slight fluctuation in the velocity recorded at monitoring point C and a prolonged deceleration time. According to kinetic energy theory, the velocity changes agreed with the landslide field landform. Furthermore, the feasibility of the proposed numerical simulation method was demonstrated.

In this work, we selected monitoring grains at the leading and trailing edges in the motion process and obtained velocity and displacement curves (Fig. 9). The overall acceleration stage occurred before 10 s, and the deceleration stage occurred after 10 s. Between 10 s and 16.5 s (Stage 1), the leading-edge velocity declined due to the impact of a hillslope on the movement path. The maximum speed of the trailing edge grains was 7 m/s, and the maximum movement distance reached 230 m. The maximum speed of the leading-edge grains was 21 m/s, and the maximum movement distance reached 830 m.

### 5.2. Case study of the Shuicheng landslide

On July 23, 2019, a long-runout landslide induced by extremely heavy rainfall occurred in Jichang town, Shuicheng County, Guizhou Province, China. Under the influence of a short-duration heavy rainfall event, a high-position sliding main body detached from a relatively steep slope and was converted into a rapid and long-runout debris flow. This flow traveled along two diversion gullies and washed out and buried houses on both sides of the valley, eventually destroying 21 houses, burying 77 people, and causing 51 deaths (Gao et al., 2020; He et al., 2022). The lithology of the rock mass was basalt. After instability occurred, the sliding main body gradually disintegrated to form basalt debris grains, which formed a two-phase mixed flow landslide through mixing with runoff. In the landslide motion process, the two-phase mixed flow was

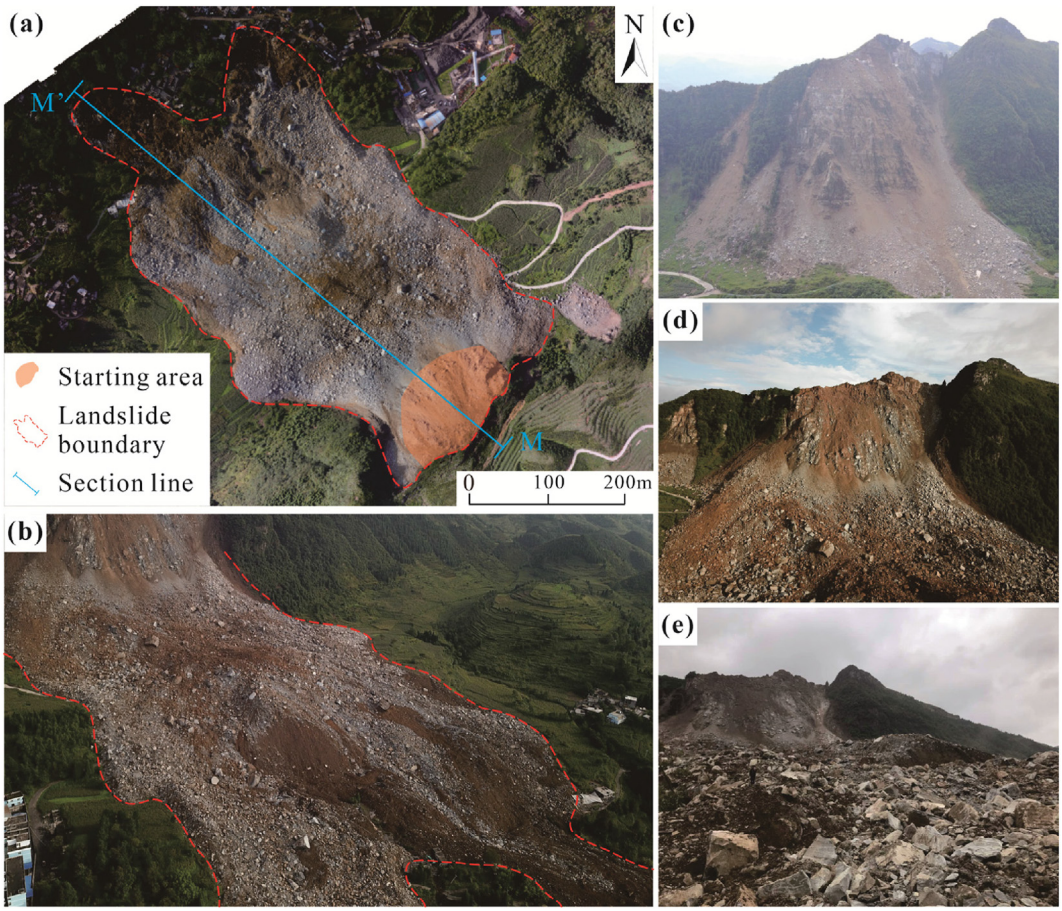


**Fig. 6.** Characteristics of the Zhangjiawan long-runout landslide deposits: (a) Remote sensing full view of the Zhangjiawan landslide, (b) Deposits at the accumulation area, (c) Front view of the source area before the avalanche, (d) Front view of the source area after the avalanche; and (e) Photos of dry debris grains.

Please cite this article as: Gao Y et al., Multistate transition and coupled solid–liquid modeling of motion process of long-runout landslide, Journal of Rock Mechanics and Geotechnical Engineering, https://doi.org/10.1016/j.jrmge.2023.12.001

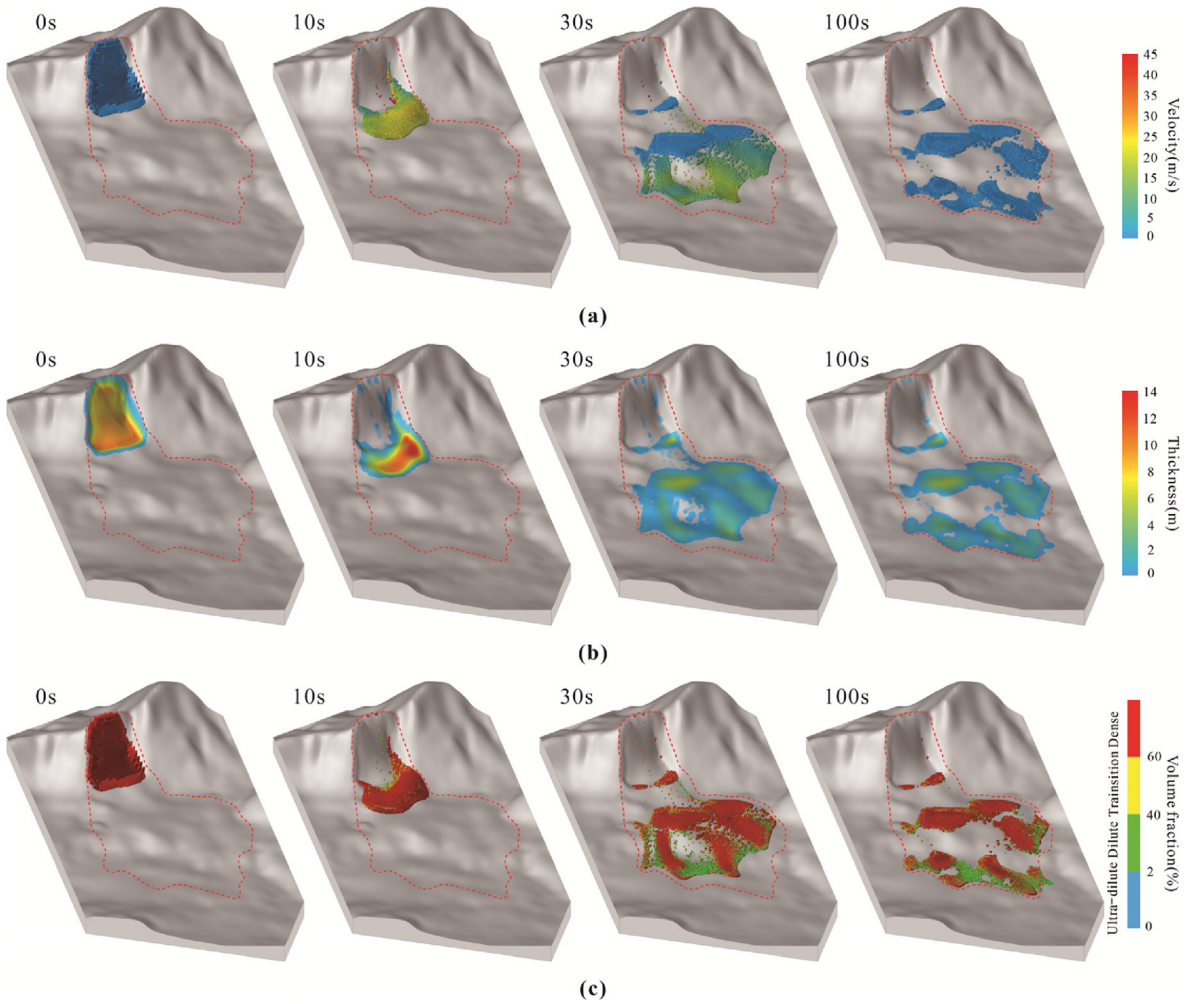


**Fig. 7.** Simulation results for the motion process of the Zhangjiawan landslide: (a) Profile of grain velocity variation at different moments, (b) Profile of the variation in accumulation thickness at different moments. The maximum accumulation thickness is located behind the hillslope, and (c) Graph of solid volume fraction results showing the state of the particles at different stages of motion.

shunted along the N5°E and N34°E directions due to obstruction by underlying microgeomorphological ridges. The deposits formed covered a maximum distance of 1340 m, with a total coverage area of $33 \times 10^4$ m$^2$ and a total volume of approximately $200 \times 10^4$ m$^3$ (Fig. 10).

The model establishment process was consistent with that of the Zhangjiawan landslide. The simulation parameters for the sliding main body material were defined based on the field parameters, the particle material was basalt debris, and the fluid was described by slurry parameters. In the two-phase coupled simulation process, the sum of the fluid and particle volume fractions equaled 100%, and the initial volume fraction of particles and fluid in the Shuicheng landslide was 50%. The influence of the fluid in the two-phase mixed flow landslide mainly included the pore water pressure and the interaction force. In the Shuicheng landslide simulation process, four working conditions were designed for the postfailure motion process (Table 4). The kinetic parameters of fluid and particle motion were determined according to landslide and field survey data (Gao et al., 2017, 2020).

The results for the four working conditions are listed in Table 5. The accumulation results for dry debris grains are shown in Fig. 11a. According to the effective stress principle, the pore water was rapidly dissipated during basalt debris particle movement. Although the landslide movement distance increased under the influence of the pore water pressure at the basal resistance boundary, it was insufficient to cause sliding at all times (Fig. 11b). Based on the fluid and solid grain interaction forces, the motion distance was significantly increased (Fig. 11c). Due to the influences of the pore water and interaction force, the simulated deposition closely approximated the landslide result (Fig. 11d). For bedrock debris grains with large voids, simulation of the motion process should focus on the influence of the interaction force. Based on multistate modeling and the LPF$^{3D}$ computing platform, the postfailure motion process of the Shuicheng landslide was modeled. The maximum velocity of individual particles at the front edge was 38 m/s. The maximum horizontal movement distance was 1360 m, which is consistent with the actual landslide. The deposition features were the same as those of the landslide (Fig. 12).

The results for the four working conditions demonstrated the important influence of the fluid on the granular flow. Fig. 13a shows a comparison of the curves of the particle velocity at the leading edge of the landslide under the four working conditions. Under the influence of the pore water and interaction force, there was a significant increase in the movement velocity of the solid particles. When the fluid was involved in the motion process, the fluid viscous force caused a more stable movement of the solid particles. Thus, the fluid deceleration phase was shorter than that of the solid particles. Fig. 13b shows a comparison of the velocity curves of the

Please cite this article as: Gao Y et al., Multistate transition and coupled solid–liquid modeling of motion process of long-runout landslide, Journal of Rock Mechanics and Geotechnical Engineering, https://doi.org/10.1016/j.jrmge.2023.12.001

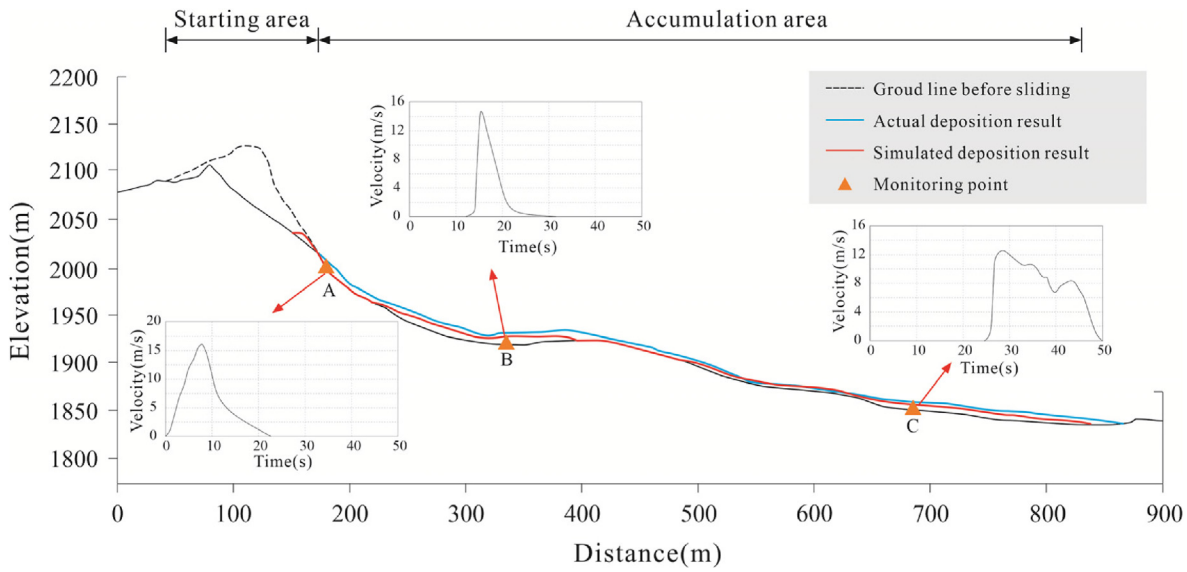


**Fig. 8.** Deposition section M-M′ and velocity monitoring curve for the Zhangjiawan landslide. The particle velocity at monitoring points A and B initially rose and then rapidly decreased. The velocity of the particles at monitoring point C first rises and then slowly decreases within 20 s.

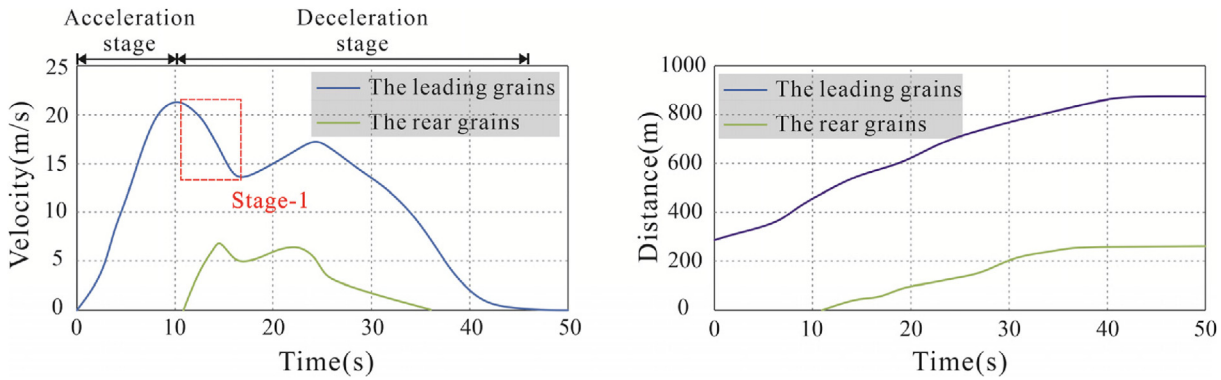


**Fig. 9.** Velocity and displacement curves of the grains at the leading and rear edges of the Zhangjiawan landslide.

solid particles and their surrounding fluids at the leading edge of the landslide under working conditions III and IV. During the initial phase, the fluid and particle velocities were the same from 0 to 10 s. Thus, the sliding main body was more notably influenced by the pore water than by the interaction forces. At the later stage, the difference between the grain and fluid velocities generated the interaction force, affecting the final movement distance.

## 6. Discussions

### 6.1. Experiments and landslide cases

Physical models also suffer limitations in terms of the size effect and similarity criterion. Landslides can hardly be replicated in lab experiments, but experiments provide the following trend discussion advantages: (a) In multistate transition dynamics modeling, the numerical parameters were based on the experimental material, which can be defined regardless of the test and landslide scales, and the repetition of the motion process and accumulation conditions was very high. The only uncertain parameter was the friction coefficient because the volume of the sliding main body greatly affects this variable (Yamada et al., 2018). (b) In solid–liquid phase coupling, we also encountered problems in the repetition of the experimental scale. The interaction model (Eq. (29)) could effectively replicate the numerical simulation results of the landslide scale, and the drag force unit mass ranged from 1 to 10 m/s$^2$. However, in the flume test, due to the small scale of the experimental device, the drag force per unit mass calculated by the numerical simulation was very small, and the experimental results could not be replicated. The repetition degree of the motion process and accumulation conditions was very high when the drag unit mass force was increased to 1–10 m/s$^2$. In summary, multistate transition and solid–liquid coupling could greatly contribute to the analysis of the landslide motion process. The numerical results were suitably validated against the flume test results and long-runout landslide cases based on LPF$^{3D}$.

### 6.2. Comparison of different numerical methods

The long-runout landslide motion process is extremely complex, and the sliding main body comprising different materials usually behaves like a solid granular flow, hyperconcentrated flow or mixed flow. Therefore, single-state constitutive models and single-phase material can hardly capture landslide movement. While a single-phase simulation model can also reproduce this process, the accuracy of this method mostly depends on the empirical equation

Please cite this article as: Gao Y et al., Multistate transition and coupled solid–liquid modeling of motion process of long-runout landslide, Journal of Rock Mechanics and Geotechnical Engineering, https://doi.org/10.1016/j.jrmge.2023.12.001


**Fig. 10.** Situation of the Shuicheng landslide: (**a**) Full view of the Shuicheng landslide, (**b**) Image of solid materials mainly composed of basalt debris of 0.1–0.3 m in diameter, and (**c**) Image of liquid materials mainly composed of slurry mixed with fine grain soil and ground runoff.

**Table 4**
LPF$^{3D}$ simulation parameters of the Shuicheng landslide.

| Working conditions | Grains phase | | | | Fluid phase (Slurry) | | |
|---|---|---|---|---|---|---|---|
| | Density (kg/m$^3$) | Grain diameter (m) | Friction coefficient | Pore pressure ratio | Density (kg/m$^3$) | Viscosity coefficient (Pa•s) | Fluid volume fraction (%) |
| I | 2800 | 0.3 | 0.5 | 0 | – | – | – |
| II | 2800 | 0.3 | 0.5 | 0.2 | – | – | – |
| III | 2800 | 0.3 | 0.5 | 0 | 1200 | 0.2 | 50 |
| IV | 2800 | 0.3 | 0.5 | 0.2 | 1200 | 0.2 | |

and parameter adjustments implemented by geologists. In this work, numerical simulation analysis of Zhangjiawan landslide and Shuicheng landslide was conducted based on different software packages and algorithms (DAN$^{3D}$, MatDEM and LPF$^{3D}$), and the simulation results are listed in Table 6 (Zhu et al., 2019; Luo et al., 2020; Zhang et al., 2020; Xia et al., 2021). Although each simulation method could be made more consistent with the landslide cases via parameter adjustment, multistate transition and solid–liquid coupling dynamics modeling more closely captured the physical process overall with over 90% accuracy using the realistic landslide parameters, and fewer particles were used to simulate realistic particle numbers, thus improving the computational efficiency.

A comparison of the results showed the following: (a) Simulation efficiency. The equivalent fluid model can attain the highest simulation efficiency, while the discrete element model attained the lowest simulation efficiency since excessive particles led to higher computer hardware requirements. The multistate transition model (LPF$^{3D}$) improved the simulation efficiency accuracy when the accuracy and stability were guaranteed; (b) Simulation result. The discrete element model focused on the collision and friction action, the motion range was dispersed, and the equivalent fluid model mainly considered the depth average false 3D simulation of the substrate shear resistance model, thereby ignoring slide internal collision, friction, and inertia. The multistate transition and solid–liquid coupling dynamics modeling method combined the advantages of the first two methods (Fig. 14); (c) Volume fraction. The multistate transition and solid–liquid coupling numerical modeling controlled the grain state through the volume fraction and reflected the internal force between grains and between phases, and the results were the closest to the landslide features. The volume fraction in this modeling is an important parameter to distinguish the grain state and solid–liquid ratio; and (d) Simulation parameters. The LPF$^{3D}$ algorithm relied on the physical and mechanical parameters of the sliding main body material. Although there are many algorithm parameters in the SPH method, they can

Please cite this article as: Gao Y et al., Multistate transition and coupled solid–liquid modeling of motion process of long-runout landslide, Journal of Rock Mechanics and Geotechnical Engineering, https://doi.org/10.1016/j.jrmge.2023.12.001

**Table 5**
Data from the actual results and simulation results of the Shuicheng landslide.

| Working conditions | Maximum velocity (m/s) | Deposition area ($km^2$) | Center of gravity distance (m) | Maximum movement distance (m) | Maximum deposition thickness (m) |
|---|---|---|---|---|---|
| I | 14 | 0.11 | 300 | 600 | 24 |
| II | 25.5 | 0.21 | 500 | 850 | 21 |
| III | 32 | 0.26 | 650 | 1000 | 23 |
| IV | 38 | 0.32 | 760 | 1360 | 21 |
| Actual landslide | 35 | 0.33 | 770 | 1340 | 20 |

be obtained through numerical tests. The physical and mechanical parameters and dynamic parameters must only be entered into the simulation model.

### 6.3. Simulation advantage

The LPF$^{3D}$ computing platform provides a new numerical simulation method to solve the multistate transition between the

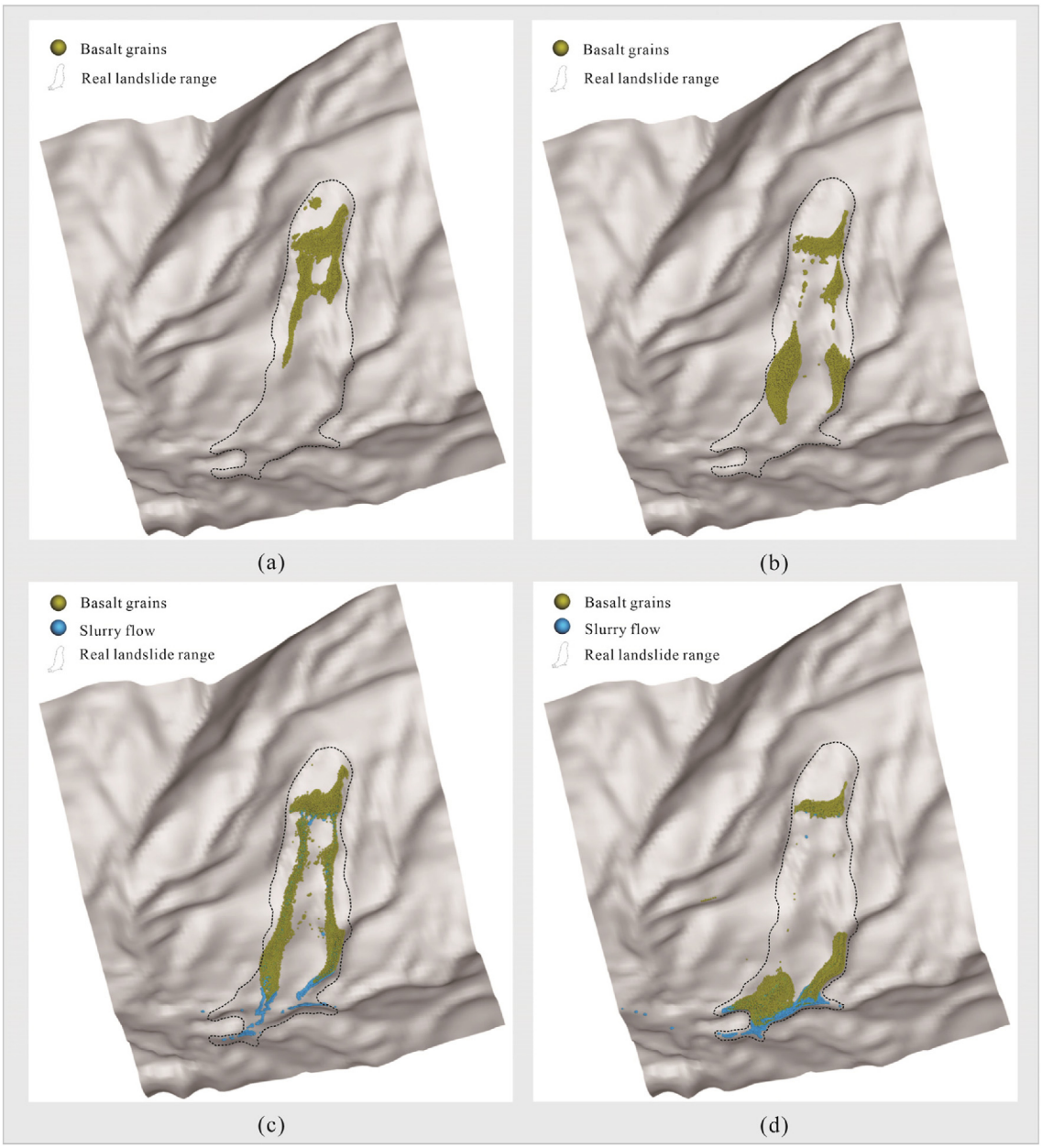


**Fig. 11.** Simulation results for the different working conditions shown in Table 4: (a) Deposition result of dry debris grains, (b) deposition result of dry debris grains with pore water pressure of the boundary layer, (c) deposition result of mixed material with 50% volume fraction of the slurry, and (d) deposition result of mixed material with 50% volume fraction of the slurry and pore water pressure of the boundary layer.

Please cite this article as: Gao Y et al., Multistate transition and coupled solid–liquid modeling of motion process of long-runout landslide, Journal of Rock Mechanics and Geotechnical Engineering, https://doi.org/10.1016/j.jrmge.2023.12.001

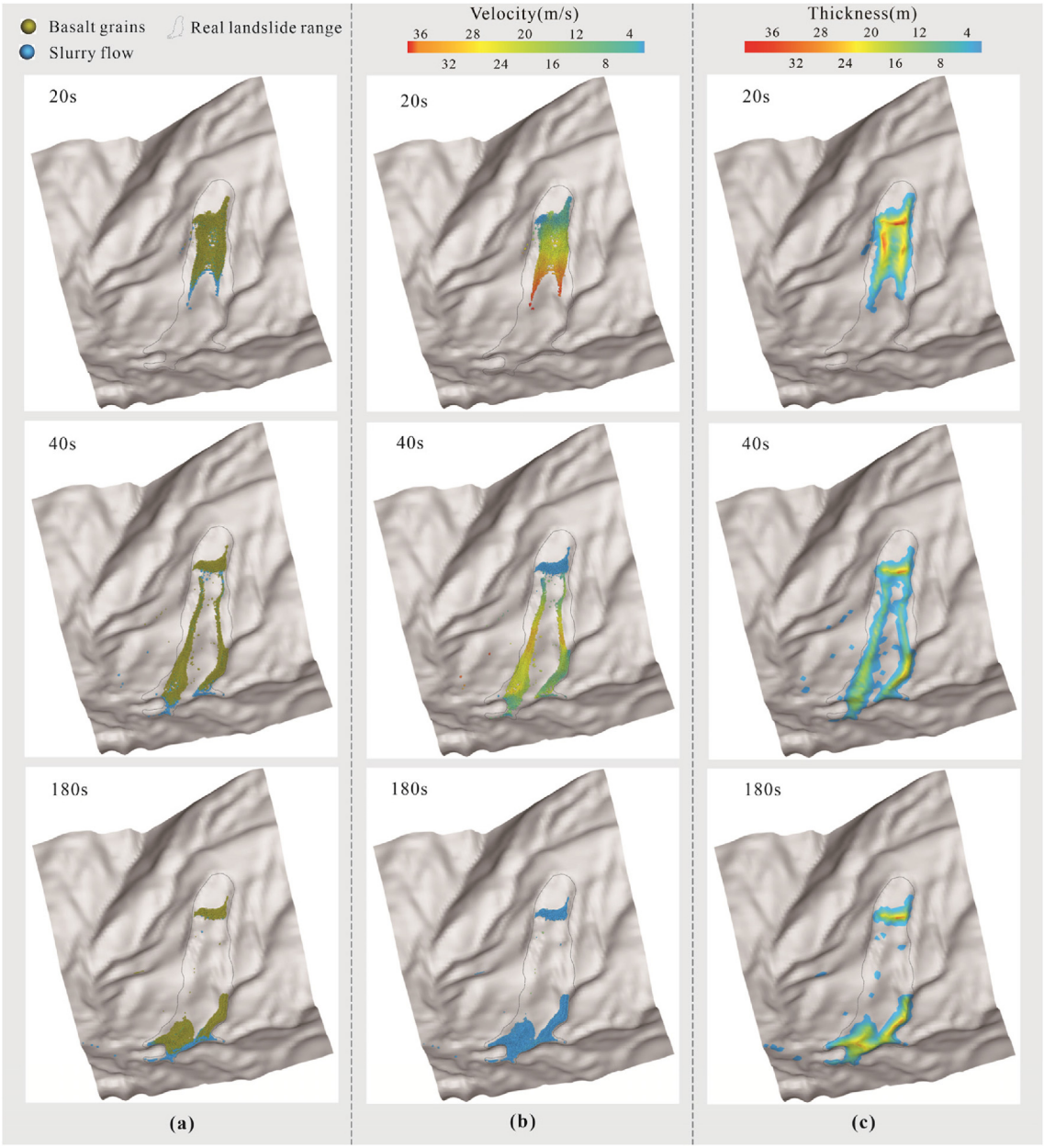


**Fig. 12.** Simulation results for the Shuicheng landslide motion process: (a) The deposition distribution results of the solid are shown in green, and the slurry is shown in blue, (b) Velocity contour map during the motion process, and (c) Deposition thickness contour map.

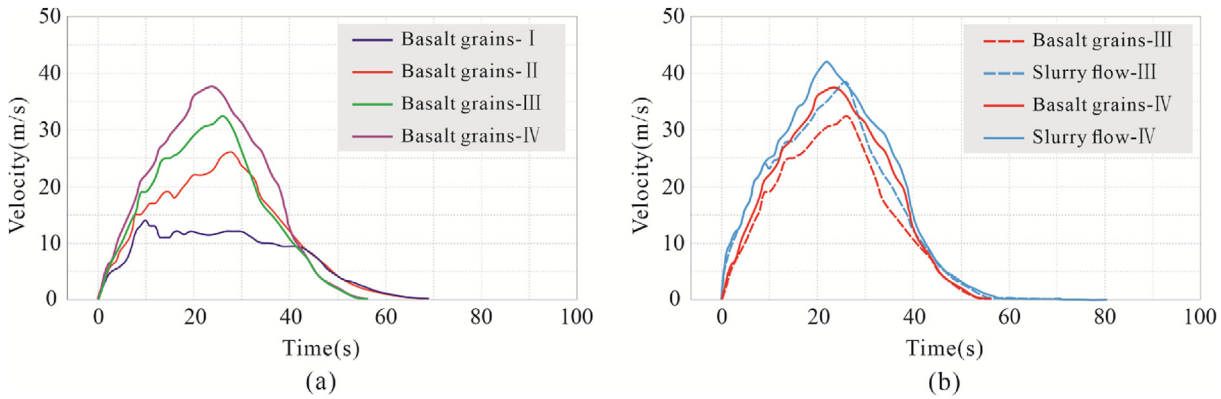


**Fig. 13.** Changes in the velocity of the grains at the front edge of the landslide under different working conditions: (a) velocity plot of basalt grains, and (b) comparison of velocity curves in conditions III and IV.

Please cite this article as: Gao Y et al., Multistate transition and coupled solid–liquid modeling of motion process of long-runout landslide, Journal of Rock Mechanics and Geotechnical Engineering, https://doi.org/10.1016/j.jrmge.2023.12.001

**Table 6**
Simulation results of the actual landslide with different numerical methods.

| References | Method | Grain size (m) | Number (numerical particles) | Maximum velocity (m/s) | Computational efficiency | Maximum distance (m) | Maximum thickness (m) |
|---|---|---|---|---|---|---|---|
| Zhangjiawan landslide | | | | | | | |
| This study | LPF$^{3D}$ | 3 | 51897 | 44 | CPU (24 core)- 12 h | 830 | 12.5 |
| Luo et al. (2020) | MatDEM | 10 | – | 40 | – | 650 | – |
| Zhu et al. (2019) | DAN$^{3D}$ | – | 2000–4000 | 40 | – | 670 | 12 |
| Actual landslide | – | | | | | 840 | – |
| **Shuicheng landslide** | | | | | | | |
| This study | LPF$^{3D}$ | 0.3 | 8860 | 38 | CPU (52 core)-90 min | 1360 | 21 |
| Xia et al. (2021) | MatDEM | 3.1–4.46 | 261700 | 44 | GPU (Tesla P100)-1080 min | 1358 | 50 |
| Zhang et al. (2020) | DAN$^{3D}$ | – | – | 40 | CPU-10 min | 1250 | 24 |
| Actual landslide | – | | | | | 1360 | 20 |

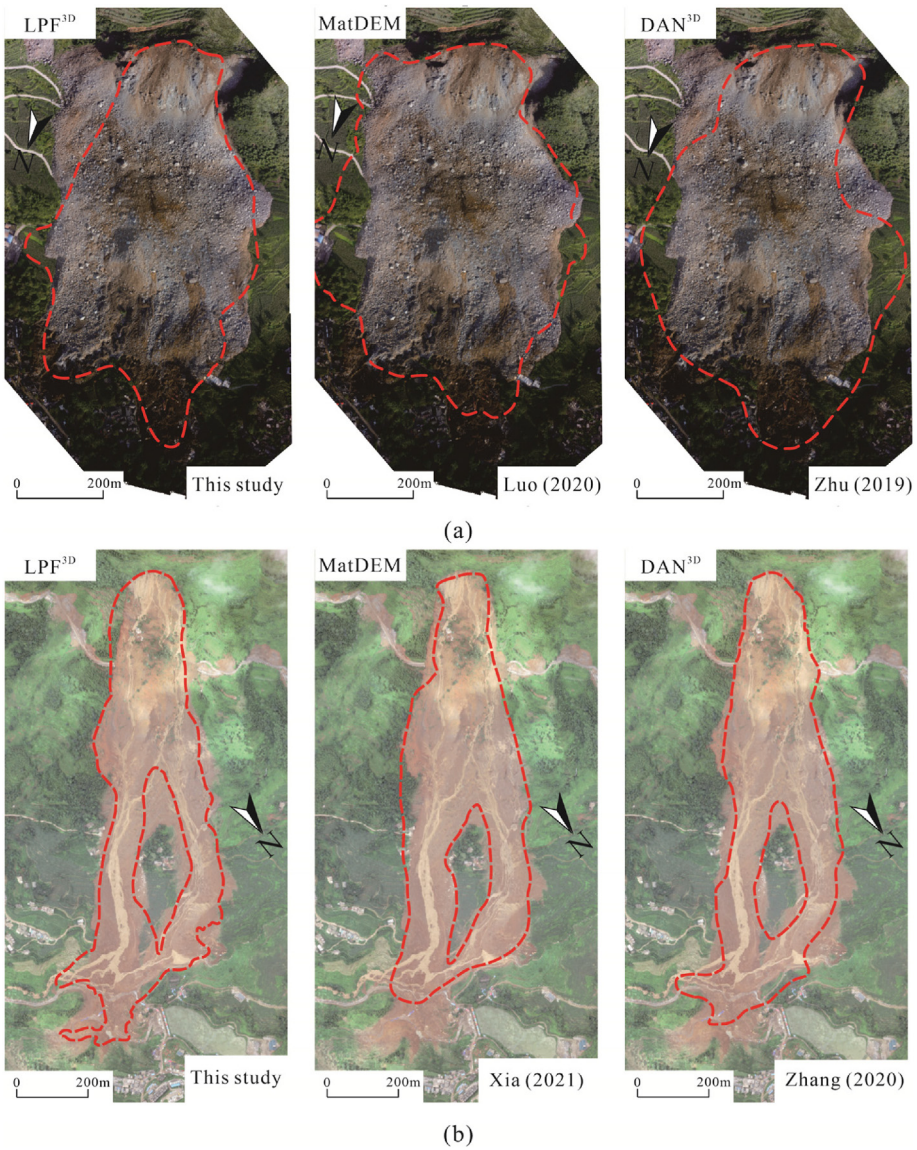


**Fig. 14.** Comparison diagram of the deposition extents of the Zhangjiawan landslide and Shuicheng landslide under different algorithm methods. The LPF$^{3D}$ method combines the advantages of a discrete media algorithm and a continuum media algorithm to improve computational accuracy and efficiency. The numerical simulation results are most consistent with the field data: (a) Zhangjiawan landslide, and (b) Shuicheng landslide.

dense, dilute and ultradilute states to achieve solid–liquid coupling, which can avoid high computational requirements, low accuracy, and difficulty in obtaining macroscopic mechanics parameters. The depositional results simulated are closest to the realistic landslide features in the multistate modeling. In terms of parameter effects, multistate transition simulations mitigated the issue of constant

Please cite this article as: Gao Y et al., Multistate transition and coupled solid–liquid modeling of motion process of long-runout landslide, Journal of Rock Mechanics and Geotechnical Engineering, https://doi.org/10.1016/j.jrmge.2023.12.001

parameters and improved the mechanical constitutive model, resulting in higher velocities and larger movement distances (Legros, 2002). This method could be used to solve the complex dynamic problems of long-runout landslide simulations with high efficiency and high precision.

## 7. Conclusions

The purpose of this study is to develop a multistate transition and solid–liquid coupling dynamics model for long-runout landslides and to provide a new numerical simulation platform ($LPF^{3D}$) for the post-failure process of long-runout landslides. The following conclusions were obtained.

(1) The motion process of a long-runout landslide entails disintegration and gradually spreading mobility with steric effects, and states mainly include dense, dilute, and ultradilute. The main macroscopic internal force in the dense state is provided by the shearing dynamic regime, that in the dilute state is provided by the collision and friction dynamic regime and that in the ultradilute state is provided by the inertial mobility dynamic regime. The dense, dilute, and ultradilute states of the granular body followed the visco-plastic constitutive model, kinetic model of granular flow, and Hertz–Mindlin contact model, respectively. The volume fraction is an important indicator to distinguish the different state types. Multistate transition and solid–liquid coupling dynamics modeling could be used to simulate the postfailure motion process with improved simulation accuracy and efficiency.

(2) A solid–liquid coupling model between the fluid phase of SPH and the grain phase of SDPH, with the simulation of the drag force between these two phases due to the velocity difference and the fluid viscosity, was built, and a fluid–solid coupling numerical simulation method was established. The volume fraction is an important indicator of the solid–liquid ratio. Numerical algorithms for the single-phase state must be used in more detailed studies of multiple-phase states and could reflect the physical and mechanical processes in debris flows.

(3) The $LPF^{3D}$ numerical simulation platform was established by combining various continuous and discrete media algorithms based on multistate transition and solid–liquid coupling theory. Similar to the single continuous media algorithm, $LPF^{3D}$ can be used to simulate the particle flow collision and friction action process with higher computational accuracy. Similar to the single discrete media algorithm, $LPF^{3D}$ can attain higher computational efficiency and accuracy. The simulation results were validated against flume experimental results and two typical long-runout landslide cases. The results effectively replicated the motion process and accumulation conditions, indicating that the proposed method can be applied to determine the landslide deposition range and evaluate the impact energy.

In multistate transition and solid–liquid coupling dynamics modeling, the $LPF^{3D}$ numerical simulation platform combined different algorithms and constitutive models to reflect the physical and mechanical processes of long-runout landslide motion, which could provide an accurate and efficient quantitative method for landslide prefailure prediction and risk assessment. The LPF3D numerical simulation platform cannot simulate and analyze the landslide scraping process. Later, the landslide scraping process will be restored utilizing the FEM.

## Declaration of competing interest

The authors declare that they have no known competing financial interests or personal relationships that could have appeared to influence the work reported in this paper.

## Acknowledgments

This research was supported by the National Science Foundation of China (Grant Nos. 42177172), and China Geological Survey Project (Grant No. DD20230538).

## List of symbols

| | |
|---|---|
| $\rho$ | density |
| $v$ | velocity |
| $\overline{v}$ | average velocity |
| $f$ | other external forces |
| $k_P$ | energy dissipation coefficient |
| $N_c\theta_P$ | energy dissipation term produced by the collisions between particles |
| $\alpha$ | volume fraction |
| $\alpha_P$ | volume fraction of the particles |
| $\alpha_f$ | fluid volume fraction |
| $\sigma$ | total stress |
| $P$ | normal stress |
| $\tau$ | friction stress |
| $c_0$ | initial velocity of sound |
| $\varepsilon$ | friction strain rate |
| $\mu$ | viscosity coefficient |
| $\dot{\sigma}$ | incremental form of the stress component |
| $G$ | friction modulus |
| $K$ | elastic modulus |
| $E$ | Young's modulus |
| $\dot{e}$ | deviatoric friction strain rate tensor |
| $\dot{\varepsilon}$ | strain rate tensor |
| $\rho_P$ | particle density |
| $g_0$ | collision recovery coefficient of the particles |
| $d_P$ | diameter of the particles |
| $e_{PP}$ | collision recovery coefficient |
| $m$ | mass |
| $t$ | time |
| $F_c$ | contact force |
| $F_d$ | viscous contact damping force |
| $k_i$ | total number of particles in contact with another particle |
| $\delta_n$ | overlap of particles at the contact |
| $k_n$ | normal stiffness |
| $E$ | Young's moduli |
| $R$ | radius |
| $\delta_t$ | friction overlap |
| $k_t$ | friction stiffness |
| $e_{pp}$ | collision recovery coefficient |
| $\beta$ | momentum transfer coefficient between the fluid and solid |
| $C_D$ | traction coefficient |
| $\varphi_P$ | internal friction angle of the solid |
| $\mu_f$ | fluid viscosity |
| $\rho_f$ | fluid density |
| $Re_P$ | relative Reynolds number |
| $\omega$ | penalty parameter |
| $r$ | radial vector |
| $W_{ij}$ | is the kernel function between grains i and j |
| $A_j$ | the area of boundary grain j |
| $r_u$ | pore pressure coefficient |

Please cite this article as: Gao Y et al., Multistate transition and coupled solid–liquid modeling of motion process of long-runout landslide, Journal of Rock Mechanics and Geotechnical Engineering, https://doi.org/10.1016/j.jrmge.2023.12.001

$\Phi$ friction angle
$H$ fluid depth

## References


Armanini, A., Fraccarollo, L., Larcher, M., 2008. Liquid-granular channel flow dynamics. Powder Technol. 182 (2), 218–227.
Bagnold, R.A., 1954. Experiments on a gravity-free dispersion of large solid spheres in a Newtonian fluid under friction. Proc. R. Soc. London, Ser. A 225 (1160), 49–63.
Banton, J., Villard, P., Jongmans, D., Scavia, C., 2009. Two-dimensional discrete element models of debris avalanches: parameterization and the reproducibility of experimental results. J. Geophys. Res.: Earth Surf. 114, F04013.
Bradley, J.B., 1986. Hydraulics and Bed Material Transport at High Fine Suspended Sediment Concentrations (Hyperconcentration, Wash Loads, Mud Flows). PhD Thesis. Colorado State University, USA.
Bryant, S.K., Take, W.A., Bowman, E.T., 2015. Observations of grain-scale interactions and simulation of dry granular flows in a large-scale flume. Can. Geotech. J. 52, 638–655.
Campbell, C.S., 1989. Self-lubrication for long runout landslides. J. Geol. 97 (6), 653–665.
Courant, R., 1943. Variational methods for the solution of problems of equilibrium and vibrations. Bull. Am. Math. Soc. 49 (1), 1–23.
Coussot, P., Meunier, M., 1996. Recognition, classification and mechanical description of debris flows. Earth Sci. Rev. 40 (3–4), 209–227.
Crosta, G.B., Imposimato, S., Roddeman, D., 2009. Numerical modelling of entrainment/deposition in rock and debris-avalanches. Eng. Geol. 109 (1–2), 135–145.
Cruden, D.M., Varnes, D.J., 1996. Landslide types and processes. Special report, transportation research board. Nat. Acad. Sci. 247, 36–75.
Chen, F., Qiang, H., Zhang, H., Gao, W., 2017. A coupled SDPH-FVM method for gas-particle multiphase flow: methodology. Int. J. Numer. Methods Eng. 109 (1), 73–101.
Chen, F., Yan, H., 2021. Constitutive model for solid-like, liquid-like, and gas-like phases of granular media and their numerical implementation. Powder Technol. 390, 369–386.
Cui, M., Chen, F., Bu, F., 2021. Multiphase theory of granular media and particle simulation method for projectile penetration in sand beds. Int. J. Impact Eng. 157, 103962.
Cundall, P.A., Strack, O.D., 1979. A discrete numerical model for granular assemblies. Geotechnique 29 (1), 47–65.
Deng, Y., He, S., Scaringi, G., Lei, X., 2020. Mineralogical analysis of selective melting in partially coherent rockslides: bridging solid and molten friction. J. Geophys. Res. Solid Earth 125, e2020JB019453.
Drame, A.S., Wang, L., Zhang, Y., 2021. Granular stack density's influence on homogeneous fluidization regime: numerical study based on EDEM-CFD coupling. Appl. Sci. 11 (18), 8696.
Evans, S.G., DeGraff, J.V., 2002. Catastrophic Landslides: Effects, Occurrence, and Mechanisms. Geological Society of America, Boulder.
Ergun, S., 1952. Fluid flow through packed columns. Chem. Eng. Prog. 48, 89–94.
Erismann, T.H., Abele, G., 2001. Dynamics of Rockslides and Rockfalls. Springer Science & Business Media.
Fan, X., Xu, Q., Scaringi, G., Zheng, G., Huang, R., Dai, L., Ju, Y., 2019. The "long" runout rock avalanche in Pusa, China, on August 28, 2017: a preliminary report. Landslides 16 (1), 139–154.
Feng, C., Li, S., Liu, X., Zhang, Y., 2014. A semi-spring and semi-edge combined contact model in CDEM and its application to analysis of Jiweishan landslide. J. Rock Mech. Geotech. Eng. 6 (1), 26–35.
Forterre, Y., Pouliquen, O., 2008. Flows of dense granular media. Annu. Rev. Fluid Mech. 40, 1–24.
Gao, Y., Li, B., Wang, G., 2016. Motion feature and numerical simulation analysis of jiweishan landslide with rapid and long run-out. J. Eng. Geol. 24 (3), 425–434 (in Chinese).
Gao, Y., Yin, Y., Li, B., Feng, Z., Wang, W., Zhang, N., Xing, A., 2017. Characteristics and numerical runout modeling of the heavy rainfall-induced catastrophic landslide–debris flow at Sanxicun, Dujiangyan, China, following the Wenchuan Ms 8.0 earthquake. Landslides 14 (4), 1361–1374.
Gao, Y., Yin, Y., Li, B., He, K., Wang, X., 2019. Post-failure behavior analysis of the Shenzhen "12.20" CDW landfill landslide. Waste Manag. 83, 171–183.
Gao, Y., Li, B., Gao, H., Chen, L., Wang, Y., 2020. Dynamic characteristics of high-elevation and long-runout landslides in the Emeishan basalt area: a case study of the Shuicheng landslide in Guizhou, China. Landslides 17 (7), 1663–1677.
Gao, Y., Yin, Y., Li, B., Wei, T., Li, Z., Gao, H., 2022. The role of fluid drag force in the dynamic process of two-phase flow-like landslides. Landslides 19, 1791–1805.
Gao, Y., Yin, Y., Li, B., Zhang, H., Wu, W., 2023. Numerical simulation method of high-position and long runout landslides under granular state transformation. J. Rock Mech. Geotech. Eng. 42 (7), 1623–1637 (In Chinese).
Gidaspow, D., 1994. Multiphase Flow and Fluidization: Continuum and Kinetic Modeling Descriptions. Academic press.
Gingold, R.A., Monaghan, J.J., 1977. Smoothed particle hydrodynamics: modeling and application to non-spherical stars. Mon. Not. Roy. Astron. Soc. 181 (3), 375–389.
Gusman, A.J., Teal, M.J., Todesco, D., Bandurraga, M., 2009. Estimating sediment/Debris bulking factors. In: Proceeding of 33rd IAHR Congress, Vancouver, British Columbia, Canada, pp. 9–14.
Handwerger, A.L., Fielding, E.J., Huang, M., Bennett, G.L., Liang, C., Schulz, W.H., 2019. Widespread initiation, reactivation, and acceleration of landslides in the Northern California Coast ranges due to extreme rainfall. J. Geophys. Res.: Earth Surf. 124, 1782–1797.
Haff, P.K., 1983. Grain flow as a fluid-mechanical phenomenon. J. Fluid Mech. 134, 401–430.
He, K., Li, J., Li, B., Gao, Y., Liu, Z., Zhao, Z., Zhao, C., 2022. The Pingdi landslide in Shuicheng, Guizhou, China: instability process and initiation mechanism. Bull. Eng. Geol. Environ. 81 (4), 1–17.
Heim, A., 1932. Der Bergsturz und Menschenleben. Fretz und Wasmuth Verlag, Zürich.
Hrennikoff, A., 1941. Solution of problems of elasticity by the framework method. J. Appl. Mech. 8 (4), 169–175.
Hungr, O., 1995. A model for the runout analysis of rapid flow slides, debris flows, and avalanches. Can. Geotech. J. 32 (4), 610–623.
Hungr, O., Evans, S.G., Bovis, M.J., Hutchinson, I.N., 2001. A review of the classification of landslides of the flow type. Bull. Assoc. Eng. Geol. 7 (3), 221–238.
Hungr, O., Dawson, R.F., Kent, A., Campbell, D., Morgenstern, N.R., 2002. Rapid flow slides of coal-mine waste in British Columbia, Canada. Geol. Soc. Am. Rev. Eng. Geol. 15, 1–18.
Hungr, O., Leroueil, S., Picarelli, L., 2014. The Varnes classification of landslide types, an update. Landslides 11 (2), 167–194.
Hutchinson, J.N., 1989. General report: morphological and geotechnical parameters of landslides in relation to geology and hydrogeology, 88-88 Int. J. Rock Mech. Min. Sci. 26 (2).
Hutter, K., Rajagopal, K.R., 1994. On flows of granular materials. Continuum Mech. Therm. 6 (2), 81–139.
Iverson, R.M., 1997. The physics of debris flows. Rev. Geophys. 35 (3), 245–296.
Iverson, R.M., Logan, M., LaHusen, R.G., Berti, M., 2010. The perfect debris flow? Aggregated results from 28 large-scale experiments. J. Geophys. Res.: Earth Surf. 115, 1–29. F03005.
Jing, L., Yang, G.C., Kwok, C.Y., Sobral, Y.D., 2019. Flow regimes and dynamic similarity of immersed granular collapse: a CFD-DEM investigation. Powder Technol. 345, 532–543.
Johnson, P.C., Nott, P., Jackson, R., 1990. Frictional–collisional equations of motion for participate flows and their application to chutes. J. Fluid Mech. 210, 501–535.
Kaitna, R., Palucis, M.C., Yohannes, B., Hill, K.M., Dietrich, W.E., 2016. Effects of coarse grain size distribution and fine particle content on pore fluid pressure and shear behavior in experimental debris flows. J. Geophys. Res.: Earth Surf. 121, 415–441.
Kelfoun, K., Giachetti, T., Labazuy, P., 2010. Landslide-generated tsunamis at Réunion Island. J. Geophys. Res.: Earth Surf. 115, 1–17. F04012.
Kim, S., Kamrin, K., 2020. Power-law scaling in granular rheology across flow geometries. Phys. Rev. Lett. 125 (8), 088002.
Larcher, M., Fraccarollo, L., Armanini, A., Capart, H., 2007. Set of measurement data from flume experiments on steady uniform debris flows. J. Hydroaul. Res. 45 (Suppl. 1), 59–71.
Legros, F., 2002. The mobility of long-runout landslides. Eng. Geol. 63 (3–4), 301–331.
Liu, C., Xu, Q., Shi, B., Deng, S., Zhu, H., 2017. Mechanical properties and energy conversion of 3D close-packed lattice model for brittle rocks. Comput. Geosci. 103, 12–20.
Li, S., Liu, W.K., 2002. Meshfree and particle methods and their applications. Appl. Mech. Rev. 55 (1), 1–34.
Louge, M.Y., 2003. Model for dense granular flows down bumpy inclines. Phys. Rev. E. 67 (6), 061303.
Louge, M.Y., Keast, S.C., 2001. On dense granular flows down flat frictional inclines. Phys. Fluids 13 (5), 1213–1233.
Luo, H., Yin, Y., Xing, A., Jin, K., Xu, S., Zhuang, Y., 2020. Characteristic analysis of the Nayong rock avalanche based on the seismic signal. In: IOP Conference Series: Earth and Environmental Science, Beijng, China.
Mezhericher, M., Brosh, T., Levy, A., 2011. Modeling of particle pneumatic conveying using DEM and DPM methods. Part. Sci. Technol. 29 (2), 197–208.
Melosh, H.J., 1986. The physics of very large landslides. Acta Mech. 64 (1), 89–99.
MiDi, G., 2004. On dense granular flows. Eur. Phys. J. E. 14, 341–365.
Monaghan, J.J., 1994. Simulating free surface flows with SPH. J. Comput. Phys. 110 (2), 399–406.
Morikawa, D.S., Asai, M., 2022. A phase-change approach to landslide simulations: coupling finite strain elastoplastic TLSPH with non-Newtonian IISPH. Comput. Geotech. 148, 104815.
Pähtz, T., Durán, O., De Klerk, D.N., Govender, I., Trulsson, M., 2019. Local rheology relation with variable yield stress ratio across dry, wet, dense, and dilute granular flows. Phys. Rev. Lett. 123 (4), 048001.
Perinotto, H., Schneider, J., Bachèlery, P., Le Bourdonnec, F., Famin, V., Michon, L., 2015. The extreme mobility of debris avalanches: a new model of transport mechanism. J. Geophys. Res. Solid Earth 120, 8110–8119.
Pudasaini, S.P., 2012. A general two-phase debris flow model. J. Geophys. Res.: Earth Surf. 117, F03010.
Pudasaini, S.P., Miller, S.A., 2013. The hypermobility of huge landslides and avalanches. Eng. Geol. 157, 124–132.


Please cite this article as: Gao Y et al., Multistate transition and coupled solid–liquid modeling of motion process of long-runout landslide, Journal of Rock Mechanics and Geotechnical Engineering, https://doi.org/10.1016/j.jrmge.2023.12.001

Qiang, H., Han, Y., Wang, K., Gao, W., 2011. Numerical simulation of water filling process based on new method of penalty function SPH. Eng. Mech. 28 (1), 245–250 (in Chinese).
Reid, M., Iverson, N., Iverson, R., LaHusen, R., Brien, D., Logan, M., 2008. Deciphering Landslide Behavior Using Large-Scale Flume Experiments. proceedings of the First World Landslide Forum, Tokyo, Japan8.
Sassa, K., Nagai, O., Solidum, R., Yamazaki, Y., Ohta, H., 2010. An integrated model simulating the initiation and motion of earthquake and rain induced rapid landslides and its application to the 2006 Leyte landslide. Landslides 7 (3), 219–236.
Scheidegger, A.E., 1973. On the prediction of the reach and velocity of catastrophic landslides. Rock Mech. 5 (4), 231–236.
Shan, T., Zhao, J., 2014. A coupled CFD-DEM analysis of granular flow impacting on a water reservoir. Acta Mech. 225 (8), 2449–2470.
Shi, G.H., 1992. Discontinuous deformation analysis: a new numerical model for the statics and dynamics of deformable block structures. Eng. Comput. 9 (2), 157–168.
Straub, S., 1996. Self-organization in the rapid flow of granular material: evidence for a major flow mechanism. Geol. Rundsch. 85 (1), 85–91.
Takarada, S., Ui, T., Yamamoto, Y., 1999. Depositional features and transportation mechanism of valley-filling Iwasegawa and Kaida debris avalanches, Japan. Bull. Volcanol. 60 (7), 508–522.
Takahashi, T., 2007. Debris Flow: Mechanics, Prediction and Countermeasures. Taylor & Francis, London.
Tan, H., Chen, S., 2017. A hybrid DEM-SPH model for deformable landslide and its generated surge waves. Adv. Water Resour. 108, 256–276.
Tan, H., Xu, Q., Chen, S., 2018. Subaerial rigid landslide-tsunamis: insights from a block DEM-SPH model. Eng. Anal. Bound. Elem. 95, 297–314.
UNESCO, 1981. Avalanche Atlas. Illustrated International Avalanche Classification. International Commission of Snow and Ice of the International Association of Hydrological Sciences, Switzerland.
UNESCO, 1993. Multilingual Landslide Glossary. The International Geotechnical Societies' UNESCO Working Party for World Landslide Inventory. BiTech Pubs, Canada.
Vallance, J.W., Scott, K.M., 1997. The Osceola Mudflow from Mount Rainier: sedimentology and hazard implications of a huge clay-rich debris flow. Geol. Soc. Am. Bull. 109 (2), 143–163.
Varnes, D.J., 1958. Landslide types and processes. In: Landslides and engineering practice, 24, pp. 20–47.
Varnes, D.J., 1978. Slope Movement Types and Processes. National Academy of Sciences, pp. 11–33.
Voight, B., Pariseau, W.G., 1978. Rockslides and avalanches: an introduction. Dev. Geotech. Eng. 14, 1–67.
Wen, C.Y., Yu, Y.H., 1966. A generalized method for predicting the minimum fluidization velocity. AIChE J. 12 (3), 610–612.
Wu, Z., Wong, L.N.Y., 2014. Underground rockfall stability analysis using the numerical manifold method. Adv. Eng. Software 76, 69–85.
Xia, G., Liu, C., Xu, C., 2021. Dynamic analysis of the high-speed and long-runout landslide motion process based on the discrete element method: a case study of the Shuicheng landslide in Guizhou, China. Adv. Civ. Eng. 2021, 1–16.
Yamada, M., Mangeney, A., Matsushi, Y., Matsuzawa, T., 2018. Estimation of dynamic friction and movement history of large landslides. Landslides 15 (10), 1963–1974.
Yang, G.C., Jing, L., Kwok, C.Y., Sobral, Y.D., 2020. Pore-scale simulation of immersed granular collapse: implications to submarine landslides. J. Geophys. Res.: Earth Surf. 125 (1), e2019JF005044.
Yin, Y., Sun, P., Zhang, M., Li, B., 2011. Mechanism on apparent dip sliding of oblique inclined bedding rockslide at Jiweishan, Chongqing, China. Landslides 8 (1), 49–65.
Yin, Y.P., Li, B., Gao, Y., Wang, W.P., Zhang, S.L., Zhang, N., 2023. Geostructures, dynamics and risk mitigation of high-altitude and long-runout rockslides. J. Rock Mech. Geotech. Eng. 15 (1), 66–101.
Zhang, L., Tang, H., Xiong, C., Huang, L., Zou, Z., 2012. Motion process simulation of high-speed long-distance jiweishan landslide with PFC3D. Chin. J. Rock Mech. Eng. 31 (S1), 2601–2611 (in Chinese).
Zhang, Y., Xing, A., Jin, K., Zhuang, Y., Bilal, M., Xu, S., Zhu, Y., 2020. Investigation and dynamic analyses of rockslide-induced debris avalanche in Shuicheng, Guizhou, China. Landslides 17 (9), 2189–2203.
Zbib, H., Ebrahimi, M., Ein-Mozaffari, F., Lohi, A., 2018. Comprehensive analysis of fluid-particle and particle-particle interactions in a liquid-solid fluidized bed via CFD-DEM coupling and tomography. Powder Technol. 340, 116–130.
Zhou, G.G.D., Li, S., Song, D., Choi, C.E., Chen, X., 2019. Depositional mechanisms and morphology of debris flow: physical modelling. Landslides 16, 315–332.
Zhou, G.G.D., Cui, K.F.E., Jing, L., Zhao, T., Song, D., Huang, Y., 2020. Particle size segregation in granular mass flows with different ambient fluids. J. Geophys. Res. Solid Earth 125 (10), e2020JB019536.
Zhu, Y., Xu, S., Zhuang, Y., Dai, X., Lv, G., Xing, A., 2019. Characteristics and runout behaviour of the disastrous 28 August 2017 rock avalanche in Nayong, Guizhou, China. Eng. Geol. 259, 105154.

**Dr. Yang Gao** received his PhD degree at the China Academy of Geosciences in 2018. He is associate research fellow of Institute of Geomechanics, Chinese Academy of Geological Sciences, China Geological Survey. He serves as a member of council of Landslide and Engineering Slope Branch, Chinese Society for Rock Mechanics & Engineering and of the research team of "World Outstanding Center for Landslide Disaster Reduction". Dr. Yang Gao has conducted the researches on the dynamics mechanism and risk mitigation of high location and long-runout landslide. He has published more than 50 academic papers, and won the "Gu Dezhen Youth Science and Technology Award", and Science and Technology Innovation Awards of Geological Society of China.

Please cite this article as: Gao Y et al., Multistate transition and coupled solid–liquid modeling of motion process of long-runout landslide, Journal of Rock Mechanics and Geotechnical Engineering, https://doi.org/10.1016/j.jrmge.2023.12.001